TAIS

Transparent Amplifying Intelligent Surface for Indoor-To-Outdoor mmWave Communications

Liu, Bin; Wang, Qing; Pollin, Sofie

DOI
10.1109/TCOMM.2023.3328259

Publication date
2024

Document Version
Final published version

Published in
IEEE Transactions on Communications

TAIS: Transparent Amplifying Intelligent Surface for Indoor-to-Outdoor mmWave Communications

Bin Liu, *Student Member, IEEE*, Qing Wang, *Senior Member, IEEE*, and Sofie Pollin, *Senior Member, IEEE*

***Abstract*— This paper presents a novel transparent amplifying intelligent surface (TAIS) architecture for uplink enhancement in indoor-to-outdoor mmWave communications. The TAIS is an amplifier-based transmissive intelligent surface that can refract and amplify the incident signal, instead of only refracting it with adjustable phase shift by most passive reconfigurable intelligent surfaces (RIS). With advanced indium tin oxide film and printing technology, TAIS can be fabricated on the windows without any visual effects. This paper primarily focuses on exploiting the TAIS-based architecture to boost the uplink spectral efficiency (SE) in indoor-to-outdoor mmWave communications. By jointly optimizing the TAIS's phase shift matrix and transmit power of the user equipment, the uplink SE can be maximized by exploiting the nonlinearity in the TAIS's amplification process. The key enabler is that we drive the optimal phase shift matrix that maximizes the SE and deduces its closed-form representation. The SE maximization is then proved to be transferred to the transmit power optimization problem. Another important enabler is that we design a low-complexity algorithm to solve the optimization problem using the difference of convex programming. Moreover, the asymptotic spectral efficiency under nonlinear amplification and power scaling law with infinitely large elements under both the sparse and rich scattering channel models are analyzed. Simulation results show that our proposed TAIS can increase the SE by up to 24.7% as compared to its alternative methods.**

***Index Terms*— Reconfigurable intelligent surface (RIS), transparent amplifying intelligent surface (TAIS), mmWave MIMO, spectral efficiency, indoor-to-outdoor communication, nonlinear amplification.**

I. Introduction

THE advanced 5G technology is empowering our lives and various industries [1], [2]. Various applications and vertical domain expansion emerging from the evolution of mobile broadband, e.g., virtual reality and augmented reality, require beyond-5G networks to provide better uplink qualities [3], [4]. In particular, over 80% of mobile uses rely on the indoor-to-outdoor communication [5]. With the standardization efforts in the 3GPP Rel-16 and Rel-17, the millimeter wave (mmWave) frequency band is introduced as the 5G new radio (NR) to accommodate the increasing spectrum and transmission demands [6]. Thus, enhancing the uplink capability of indoor-to-outdoor mmWave communication is important for future wireless networks.

Enhancing the uplink capability in indoor-to-outdoor mmWave communication is challenging. One reason is that the radio waves from indoors to outdoors suffer from penetration losses greatly, in the order of 15 to 26 dB in sub-6 GHz and 35 to 53 dB for mmWave band [7]. Another reason is that UEs are powered by battery, and the additional penetration loss challenges the link budget of indoor UEs. Emerging applications such as extended reality (XR) have the requirements in both capacity and power saving as specified in 3GPP Rel-17 [8]. It is critical to boost the uplink capacity with efficient power saving of UEs for indoor-to-outdoor communication.

Relay or repeater, a node deployed between the base station (BS) and UEs, can improve the network capacity in buildings. 3GPP standardizes relays for different 5G use case scenarios, such as integrated access and backhaul in Rel-16 and Rel-17. However, relaying has several drawbacks, such as signal processing complexity, noise enhancement, and self-interference at the relay nodes. Thanks to the advances in meta-materials, reconfigurable intelligent surfaces (RISs) have been proposed to intelligently control the wireless channels [9], [10], [11]. Passive RIS elements are man-made electromagnetic sensors that are controlled by integrated circuits to effectively adapt the wavefront characteristics such as phase, frequency, and even polarization of impinging signals. Due to these advantages, RIS has become a promising technology for beyond-5G networks [12]. Compared to traditional amplify-and-forward relays, RISs have low complexity and self-interference avoidance advantages. Without requiring completed RF modules, most RISs reflect or passively refract impinging signals. Moreover, RISs are configured to operate as anomalous reflectors or refactors that are not subject to the half-duplex constraint and self-interference, which typically exist in the amplify-and-forward relays. RIS has been studied in [13] to enhance indoor-to-outdoor communication, where the RIS is composed of a large number of chipless RFID sensors and built inside the wall with outdoor and indoor antennas on both sides.

However, RIS can introduce the *multiplicative fading* effect, because the equivalent path loss between the transmitter-RIS-receiver link is the product of the path losses of the transmitter-RIS and RIS-receiver links, which could be much

Manuscript received 20 October 2022; revised 16 March 2023 and 1 September 2023; accepted 19 October 2023. Date of publication 3 November 2023; date of current version 16 February 2024. An earlier version of this paper was presented in part at the IEEE International Conference on Communications, Rome, Italy, May 2023 [DOI: 10.1109/ICC45041.2023.10279668]. The associate editor coordinating the review of this article and approving it for publication was N. G. Gonzalez-Prelcic. *(Corresponding author: Bin Liu.)*

Bin Liu and Sofie Pollin are with the Department of Electrical Engineering, KU Leuven, 3000 Leuven, Belgium (e-mail: liubinkul@outlook.com).

Qing Wang is with the Department of Computer Science, Delft University of Technology, 2628 CD Delft, The Netherlands.

Color versions of one or more figures in this article are available at https://doi.org/10.1109/TCOMM.2023.3328259.

Digital Object Identifier 10.1109/TCOMM.2023.3328259

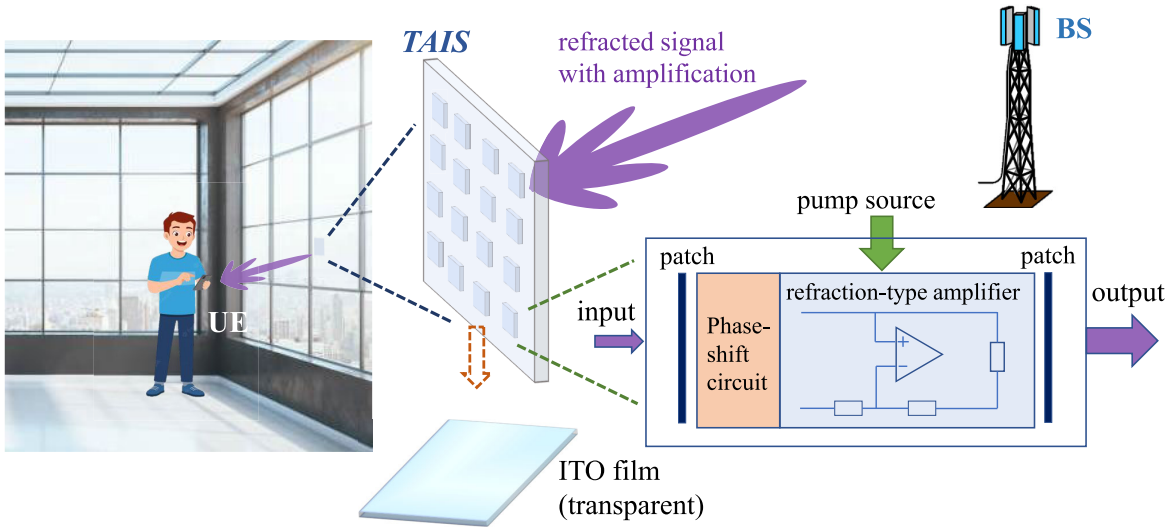

Fig. 1. Illustration of the proposed TAIS-enhanced indoor-to-outdoor mmWave communications.

larger than that of the direct link [14], [15], [16]. To overcome this issue, Long et al. in [17] use active RIS where each element is assisted by active loads that reflect and amplify the incident signal. In [18], reflection-type power amplifiers (PAs) are integrated into RIS to amplify the reflected signals. However, most of the current active RIS studies evaluate the performance under the linear amplification process assumption. In practice, the amplification of PA is always *nonlinear*. When working in a saturation regime, PAs generate distortion – which is relevant to the input signal – and degrades the system performance.

In this paper, for the first time, we propose a *transparent amplifying intelligent surface (TAIS)* architecture for the indoor-to-outdoor mmWave communications, as illustrated in Fig. 1. This amplifier-based transmissive metasurface can refract and amplify the incident signal instead of only refracting it with the adjustable phase shift. Benefiting from the advanced indium tin oxide (ITO) film and printing technologies, TAIS can be fabricated on an *optically-transparent* ITO glass or graphene materials [19], [20], which can be integrated into the windows without visual effects [21]. TAIS could be easily installed in an environment-friendly way and can match the surroundings, rather than being embedded into/on concrete walls like some RISs [13]. To analyze the TAIS's performance, we select the metric *uplink spectral efficiency (SE)* with the practical consideration of nonlinear amplification. The SE maximization objective is formulated by jointly optimizing the phase shift matrix of the TAIS and the transmit power of the UE. Below, we summarize the main contributions of this paper.

- We propose a first-of-its-kind transparent amplifying intelligent surface (TAIS) architecture for uplink enhancement of the indoor-to-outdoor mmWave communications. As an optically-transparent refractor that can be deployed on windows, TAIS can adjust the phase shift of impinging signals, perform beamforming and amplify the signals. Thus, TAIS can save the link budget of indoor UEs.
- We drive the optimal phase shift matrix that maximizes the uplink spectral efficiency and deduces its closed-form representation, where the PAs' nonlinearity is considered in the amplification process of TAIS. The SE maximization is proved to be transferred to the optimal transmit power optimization problem. We further design a low-complexity algorithm to obtain the optimal transmit power based on the difference of convex (DC) programming.
- We analyze the asymptotic SE considering the nonlinearity of the PAs under both sparse and rich scattering channel models. We also examine the power scaling law of the TAIS-enhanced mmWave communication when there are an infinite number of elements.

Through various simulations we demonstrate that our proposed TAIS-enhanced indoor-to-outdoor mmWave communication can enhance the uplink capacity without sacrificing the link budgets of UEs. Simulation results show that our algorithm can achieve an SE increase of up to 24.7% when compared to other alternative methods.

The rest of this paper is organized as follows. Section II describes the architecture and models of the proposed TAIS. Section III formulates the considered SE maximization objective. Section IV elaborates on the joint phase shift matrix and transmit power optimization. Asymptotic spectral efficiency analysis is given in Section V. Simulation results and conclusion are presented in Section VI and Section VII, respectively.

Notations: The following notations are used throughout this paper. $\mathbf{a}$ and $\mathbf{A}$ stand for a column vector and a matrix, respectively; $[\mathbf{A}]_{i,j}$ is the entry on the ith row and jth column of $\mathbf{A}$. The conjugate, transpose, conjugate transpose, determinant, and trace of $\mathbf{A}$ are represented by $\mathbf{A}^*$, $\mathbf{A}^T$, $\mathbf{A}^H$, $\det(\cdot)$ and $tr(\cdot)$, respectively; $|\cdot|$ and $\|\cdot\|$ denote modulus and Frobenius norm, respectively; $\odot$ denotes the element-wise

product operation of a matrix; $\mathbb{E}[\cdot]$ is the expectation of a complex variable; $\mathbb{C}$ and $\mathbb{N}$ represent the complex number and nature number, respectively; $\mathcal{CN}(\bar{\mu}, \mathbf{\Sigma})$ denotes the complex multivariate Gaussian distribution with mean $\bar{\mu}$ and variance $\mathbf{\Sigma}$.

II. TAIS-Enhanced Indoor-to-Outdoor mmWave Communication

A. System Model

We consider a TAIS-enhanced indoor-to-outdoor mmWave communication system as shown in Fig. 1. The optical-transparent TAIS is deployed on the window to enhance the performance of the uplink mmWave transmission from the indoor UE to the outdoor BS. Because the TAIS is transparent, it does not affect much the visual effect of the window. Assume the BS is equipped with N receiving antennas and the UE has a single antenna. There are M active transmissive elements (TE) on the TAIS, where each element can reconfigure the incident signal from the UE with the desired phase shift and amplify the signal. The signal amplification is realized by a parametric power amplifier [22]. Let the diagonal matrix $\mathbf{\Theta} = \text{diag}(e^{\jmath\vartheta_1}, \cdots, e^{\jmath\vartheta_M}) \in \mathbb{C}^{M\times M}$ denote the phase shift matrix of the TAIS, where $\vartheta_m \in [0, 2\pi)$ is the phase shift of the TAIS's m-th element. The baseband equivalent channels from the UE to the TAIS, and from the TAIS to the BS, are denoted by $\mathbf{h} \in \mathbb{C}^{M\times 1}$ and $\mathbf{F} \in \mathbb{C}^{N\times M}$, respectively. Following the state-of-the-art studies [15], [16], [17], [18], we assume the channel state information (CSI) of all the involved channels is known at the UE, BS, and TAIS. The received signal at the BS is given by

$$\mathbf{r} = \mathbf{F} f_A(\mathbf{\Theta}\mathbf{h}s) + \mathbf{n} = \mathbf{F} f_A(\mathbf{\Theta}\mathbf{x}) + \mathbf{n}, \tag{1}$$

where $\mathbf{x} = \mathbf{h}s = [x_1, \cdots, x_M] \in \mathbb{C}^{M\times 1}$ denotes the incident signal at the TAIS; s is the transmitted signal by the UE with transmit power $\mathbb{E}[|s|^2] = P$; $f_A(\cdot) : \mathbb{C} \to \mathbb{C}$ is a function that describes the input and the output relationship of the signal amplification process at the TAIS; $\mathbf{n} \sim \mathcal{CN}(0, N_0\mathbf{I}_N)$ models the additive circularly symmetric complex Gaussian noise. We present the modulation and application process of the TAIS and channel modelling for the considered TAIS-aided indoor-to-outdoor mmWave communication scenario in the following subsections.

Remark: Note that our proposed TAIS is fundamentally different from the hybrid relay-reflecting RIS described in [23], [24], [25], and [26]. Specifically, each element in the hybrid relay-reflecting RIS connects to a complete RF component including the power amplifier and RF chain, enabling the digital modulation of the signal in both amplitude and phase. Such active elements of a relay-reflecting RIS are used for sending pilot signals and estimating the channel state information [23], [24], [25], or performing digital beamforming [26]. In contrast, our proposed TAIS is simpler, which does not perform fully digital modulation but only refracts and amplifies the incident signals. The signal amplification mechanism of TAIS is similar to the reflect-type amplifying surface [18], [27], but TAIS is in a *refraction* manner. TAIS is also different from the full-duplex amplify-and-forward relay, in terms of hardware architecture and transmission model. Specifically, a full-duplex amplify-and-forward relay is equipped with RF chains to receive the incident signal and then transmit it after amplification in two successive slots. Our TAIS, based on the amplification metasurface [28], [29], provides directive and diverse radiation beams and large amplification, and steer beams by simply changing the bias of the gradient active nonmagnetic nonreciprocal phase shifters.

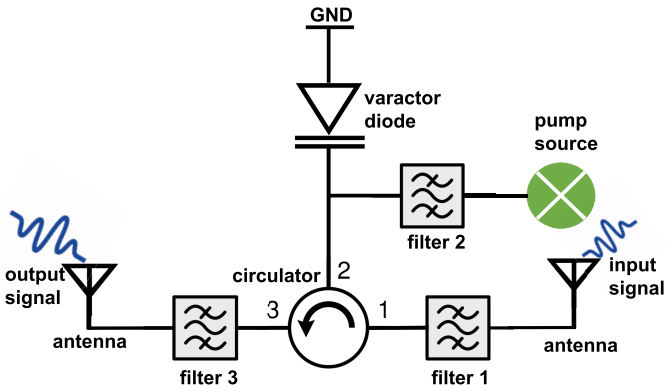

Fig. 2. Block diagram of a refraction-type amplifier.

B. Transmissive Amplifying Surface Model

Each element in the proposed TAIS can work as a refraction-type amplifier, which allows the refraction coefficient η greater than unity, i.e.,

$$|\eta|^2 = \frac{(R_L + R_A)^2 + (X_L + X_A)^2}{(R_L - R_A)^2 + (X_L + X_A)^2} > 1, \tag{2}$$

where R_L and R_A denote the resistance of the load and the antenna, respectively; X_L and X_A denote the reactance of the load and the antenna, respectively. It enables the elements to serve as low-power refraction-type amplifiers.

The low-power refraction amplifier, whose block diagram is illustrated in Fig. 2, can realize the power amplification with a varactor diode circuit, three filters, and a pump source. An ideal impedance matching can be employed to realize such a single-port amplifier. The input signal power is amplified at the varactor diode, which can form a parametric amplifier based on the Manley–Rowe relations [30]. Filter 1 works for filtering out the undesired signal spectrum. Filter 2 works for the ideal operation of parametric amplification. In particular, it only allows the signal at the frequency of the pump source to pass through, which prevents mixing the input signal or the high-frequency component generated during the amplification process into the pump source. Filter 3 is used to filter out the undesired high-frequency component in the amplification, and only the amplified input signal at f_0 can pass through. The circulator can discriminate the input signal and the output signal during the amplification process. In addition, due to the nonlinear property of the varactor diode, there exists a nonlinear operation region where the amplification gain is nonlinear while the phase is almost perfectly preserved [17]. Next, we model the nonlinear amplification process.

C. Nonlinear Amplification Model

In this paper, we adopt a memoryless polynomial model of order $2K+1$ to describe the nonlinear behaviour of the power amplification process $f_A(\cdot)$, following [31], [32], and [33]. The equivalent baseband output signal of the m-th PA connected to the TE is given by

$$u_m = f(v_m) \triangleq \sum_{k=0}^{K} \beta_{2k+1} |v_m|^{2k} v_m, \tag{3}$$

where $v_m = [\mathbf{\Theta}]_{m,m} h_m s$ denotes the equivalent phase-modulated signal of the m-th TE. β_{2k+1} is a model parameter that takes complex values in general. It can capture both amplitude-to-amplitude modulation (AM/AM) distortion and amplitude-to-phase modulation (AM/PM) distortion. The instantaneous amplitude gain of the PA is written as

$$g_m \triangleq \frac{u_m}{v_m} = \sum_{k=0}^{K} \beta_{2k+1} |v_m|^{2k}. \tag{4}$$

Let the diagonal matrix $\mathbf{G} = \mathrm{diag}(g_1, \cdots, g_M)$ denote the instantaneous amplitude gain of each PA in (4), and phase-modulated signal vector is denoted by $\mathbf{v} = [v_1, \cdots, v_M]^{\mathrm{T}} = \mathbf{\Theta h} s \in \mathbb{C}^{M\times 1}$ Then, the amplified signal vector $\mathbf{u}$ can be represented as $\mathbf{u} = \mathbf{G v}$.

D. Channel Model

1) Outdoor Channel Model: We consider a cluster channel model with L_2 paths in the outdoor scenario between the TAIS and the BS, and the channel matrix can be given by

$$\mathbf{F} = \sqrt{\frac{MN}{L_2}} \sum_{\ell=1}^{L_2} \alpha_\ell \mathbf{a}_{\mathrm{BS}}(\psi_\ell^B, \phi_\ell^B) \mathbf{a}_{\mathrm{TAIS}}^{\mathrm{H}}(\psi_\ell^{S_t}, \phi_\ell^{S_t}) \in \mathbb{C}^{N\times M}, \tag{5}$$

where α_ℓ is the complex gain of path ℓ between the TAIS and the BS, which includes both the path-loss and small-scale fading. In particular, for the given large-scale fading, $\{\alpha_\ell\}$ for all $\ell \in \{1, \cdots, L_2\}$ are i.i.d. random variables drawn from distribution $\mathcal{CN}(0, 10^{-0.1\mathrm{PL}_2})$, where PL_2 is the outdoor path-loss in dB, consisting of a constant attenuation, a distance-dependent attenuation, and a large-scale log-normal fading. ψ_ℓ^B and ϕ_ℓ^B are the azimuth and elevation angles of arrival (AoA) of the BS; $\psi_\ell^{S_t}$ and $\phi_\ell^{S_t}$ are the azimuth and elevation angles of departure (AoD) of the TAIS, respectively, corresponding to the channel's path ℓ. $\mathbf{a}_{\mathrm{TAIS}} \in \mathbb{C}^{M\times 1}$ and $\mathbf{a}_{\mathrm{BS}} \in \mathbb{C}^{N\times 1}$ are the unit-norm array response vectors of the BS and TAIS arrays, respectively. We assume that both the BS and TAIS are equipped with uniform planar arrays (UPAs) [34]]with array responses

$$\mathbf{a}_{\mathrm{BS}}(\psi, \phi) = \frac{1}{\sqrt{N_{az} N_{ev}}} \Big[1, \cdots, e^{-\jmath \frac{2\pi}{\lambda} \Delta_r (n_a \sin\psi \sin\phi + n_b \cos\phi)}, \cdots, e^{-\jmath \frac{2\pi}{\lambda} \Delta_r ((N_{az}-1)\sin\psi \sin\phi + (N_{ev}-1)\cos\phi)}\Big]^T, \tag{6}$$

$$\mathbf{a}_{\mathrm{TAIS}}(\psi, \phi) = \frac{1}{\sqrt{M_{az} M_{ev}}} \Big[1, \cdots, e^{-\jmath \frac{2\pi}{\lambda} \Delta_t (m_a \sin\psi \sin\phi + m_b \cos\phi)}, \cdots, e^{-\jmath \frac{2\pi}{\lambda} \Delta_t ((M_{az}-1)\sin\psi \sin\phi + (M_{ev}-1)\cos\phi)}\Big]^T, \tag{7}$$

where N_{az} and N_{ev} (or M_{az} and M_{ev}) are the number of elements on each column and the row of the UPA at BS or TAIS, respectively; we have $N = N_{az} N_{ev}$ and $M = M_{az} M_{ev}$. λ is the signal wavelength. Δ_t and Δ_r represent the antenna spacing of the arrays at the TAIS and BS, respectively.

2) Indoor Channel Model: We consider a cluster channel model with L_1 paths between the TAIS and the UE in the indoor scenario. The channel matrix can be given by

$$\mathbf{h} = \sqrt{\frac{M}{L_1}} \sum_{\ell=1}^{L_1} \zeta_\ell \mathbf{a}_{\mathrm{TAIS}}(\psi_\ell^{S_r}, \phi_\ell^{S_r}) \in \mathbb{C}^{M\times 1}, \tag{8}$$

where ζ_ℓ is the complex gain of path ℓ between the TAIS and the UE, which includes both the path-loss and small-scale fading. In particular, for the given large-scale fading, $\{\zeta_\ell\}$ for all $\ell \in \{1, \cdots, L_1\}$ are i.i.d. random variables drawn from distribution $\mathcal{CN}(0, 10^{-0.1\mathrm{PL}_1})$, where PL_1 is the indoor path-loss in dB. $\psi_\ell^{S_r}$ and $\phi_\ell^{S_r}$ are the azimuth and elevation angles of arrival of the TAIS, corresponding to path ℓ of the channel, respectively.

III. Problem Formulation

In this section, we analyze the uplink spectral efficiency (SE) of the proposed TAIS-enhanced indoor-to-outdoor mmWave communication system, where a realistic amplification process of TAIS is considered. In particular, by applying Bussgang's theorem [34], we divide the amplified signal into two parts: a linear scaled part and an uncorrelated distortion part. The SE of the nonlinear amplification at TAIS is derived. Finally, the SE maximization problem is formulated by jointly optimizing the phase shift matrix of the TAIS and the transmit power of the UE.

Based on Bussgang's theorem, the amplified signal of TAIS can be represented as

$$\mathbf{u} = \overline{\mathbf{G}}\, \mathbf{v} + \mathbf{e} \in \mathbb{C}^M, \tag{9}$$

where $\mathbf{v}$ is the linearly amplified version of the phase modulated signal at TAIS, and contaminated with the nonlinear distortion $\mathbf{e}$. $\overline{\mathbf{G}}$ denotes the average linear gain of the amplification. $\mathbf{e} = [e_1, \cdots, e_M]$ collects the nonlinear distortion over all the elements. According to the Bussgang's theorem, the distortion generated at the output of each PA is uncorrelated with the input signal to that PA, i.e., $\mathbb{E}\{v_m^* e_m\} = 0$. We assume that the element branches are isolated from each other. Hence, $\overline{\mathbf{G}}$ is assumed to be a diagonal matrix and can be given as

$$\overline{\mathbf{G}} = \mathrm{diag}\left(\overline{g}(\rho_1), \cdots, \overline{g}(\rho_m)\right), \tag{10}$$

where $\rho_m = |h_m e^{\jmath \vartheta_m}|^2 P$ is the power of the input signal at m-th PA; $\overline{g}(\rho_m) = \sum_{k=0}^{K} \beta_{2k+1} (k+1)! |^{2k} \rho_m{}^k$ is the linear amplification gain. The derivation details can be found

in Appendix A. Then, by comparing with $\mathbf{u} = \mathbf{G}\mathbf{v}$ in (4), the nonlinear distortion can be expressed as

$$\mathbf{e} = \left(\mathbf{G} - \overline{\mathbf{G}}\right)\mathbf{v}, \tag{11}$$

where the distortion vector $\mathbf{e}$ is a zero-mean complex random vector with covariance matrix as

$$\mathbf{C_e} = \sum_{k=1}^{K} \mathbf{\Gamma}_k \mathbf{C_v} \odot |\mathbf{C_v}|^{2k} \mathbf{\Gamma}_k^H, \tag{12}$$

where $\mathbf{C_v} = \mathbb{E}\{\mathbf{v}\mathbf{v}^{\mathrm{H}}\} = P\mathbf{\Theta}\mathbf{h}\mathbf{h}^{\mathrm{H}}\mathbf{\Theta}^{\mathrm{H}}$ is the covariance matrix of signal vector $\mathbf{v}$. $\mathbf{\Gamma}_k = \mathrm{diag}\left(\gamma_k\left(P_1\right), \cdots, \gamma_k\left(P_M\right)\right)$ and

$$\gamma_k(\rho_m) = \sqrt{\frac{1}{k+1}} \sum_{q=k}^{K} \beta_{2k+1} \binom{q}{k} (q+1)! \left(|h_m e^{j\vartheta_m}|^2 P\right)^{(q-k)}. \tag{13}$$

The detailed derivation can be found in Appendix B.

Incorporating the PA's nonlinearity, the received signal at the BS in (1) is updated as

$$\mathbf{r} = \mathbf{F}\overline{\mathbf{G}}\mathbf{v} + \mathbf{F}\mathbf{e} + \mathbf{n}. \tag{14}$$

When Gaussian symbols are transmitted, the SE of the uplink transmission is given by

$$\begin{aligned} SE &= \log_2\left[\det\left(\mathbf{I}_N + \mathbf{R}_{\mathbf{n}}^{-1}\mathbf{F}\overline{\mathbf{G}}\mathbf{C_v}\overline{\mathbf{G}}^{\mathrm{H}}\mathbf{F}^{\mathrm{H}}\right)\right] \\ &= \log_2\left[\det\left(\mathbf{I}_N + P\mathbf{R}_{\mathbf{n}}^{-1}\mathbf{F}\overline{\mathbf{G}}\mathbf{\Theta}\mathbf{h}\mathbf{h}^{\mathrm{H}}\mathbf{\Theta}^{\mathrm{H}}\overline{\mathbf{G}}^{\mathrm{H}}\mathbf{F}^{\mathrm{H}}\right)\right], \end{aligned} \tag{15}$$

where $\mathbf{R_n} = \mathbf{F}\mathbf{C_e}\mathbf{F}^{\mathrm{H}} + N_0\mathbf{I}_N$.

As derived in (10) and (12), the linear amplification matrix $\overline{\mathbf{G}}$ and the covariance matrix of the distortion $\mathbf{C_e}$ depend on both the phase shift matrix $\mathbf{\Theta}$ of the TAIS and the transmit power P of the UE. Hence, the optimization problem is formulated as maximizing the SE by jointly optimizing the phase shift matrix of the TAIS and the transmit power of the UE, as follows:

$$\mathcal{P}_0: \max_{P,\mathbf{\Theta}} \quad SE(P, \mathbf{\Theta}) \tag{16a}$$

$$\text{s.t.} \quad 0 \le P \le P_{\max}, \tag{16b}$$

$$\mathbf{\Theta} = \mathrm{diag}\left(e^{j\vartheta_1}, e^{j\vartheta_2}, \cdots, e^{j\vartheta_M}\right), \tag{16c}$$

where $P_{\max}$ is the maximum transmit power of the UE.

IV. Uplink SE Optimization

Problem $\mathcal{P}_0$ is challenging due to the nonconvexity of the objective function and the per-element unit modulus constraint placed on the phase shift matrix of the TAIS. In particular, due to the absence of distortion $\mathbf{C_e}$ in (12) and per-element unit modulus constraint, $\mathcal{P}_0$ is a non-convex optimization problem with non-convex constraints. Furthermore, the computation of the distortion covariance matrix $\mathbf{C_e}$ incurs high complexity due to the high-order element-wise matrix product. In this section, we will derive the optimal phase shift matrix $\mathbf{\Theta}^*$ that maximizes SE under the considered indoor-to-outdoor scenario. Then, the SE maximization problem $\mathcal{P}_0$ is proved to be transferred to the optimal transmit power optimization problem. Finally, to further reduce the computational complexity, we design a low-complexity algorithm to obtain the solution using the difference of convex (DC) programming.

Considering in reality that the indoor distance d_1 is usually short, the maximum clearance of the first Fresnel zone can be written as [35]

$$d_F = \frac{1}{2}\sqrt{d_1\lambda}. \tag{17}$$

For example, at the typical mmWave frequency $f = 28$ GHz, the maximum clearance of the first Fresnel zone $d_F \approx 7.32$ mm for a typical indoor distance $d_1 = 2$ m. The surface with $M = 1000$ elements is about 8 mm in length, which means the power of the incidence signal on the surface is dominated by the strongest path of the indoor channel $\mathbf{h}$. Moreover, as indicated in the 3GPP clustered-delay-line (CDL) models [36], although multiple clusters may exist in the channel, the directed and narrow beam makes clusters in the other directions insignificant to the communication link. This dominant cluster or path concept has also been verified recently by a dynamic mmWave channel measurement in an indoor scenario at 28–30 GHz [37]. With these observations, the indoor channel characteristics can be approximately represented by its strongest path, as given by

$$\mathbf{h} \approx \sqrt{M}\zeta_{\max}\mathbf{a}_{\mathrm{TAIS}}(\overline{\psi}_{\max}^{S_r}, \overline{\phi}_{\max}^{S_r}) \triangleq \sigma_h\overline{\mathbf{h}} \in \mathbb{C}^{M\times 1}, \tag{18}$$

where $\psi_{\max}^{S_r}, \phi_{\max}^{S_r}$ are the azimuth and elevation angles of arrival at the TAIS that correspond to the strongest path with the largest channel gain $\zeta_{\max}$ in the indoor channel $\mathbf{h}$. For notation simplicity, let the complex channel gain $\sigma_h = \sqrt{M}\zeta_{\max}$, and $\overline{\mathbf{h}} = \mathbf{a}_{\mathrm{TAIS}}(\overline{\psi}_{\max}^{S_r}, \overline{\phi}_{\max}^{S_r})$. Then, the covariance matrix of the phase-modulated signal $\mathbf{v}$ can be written as

$$\begin{aligned} \mathbf{C_v} &= \mathbb{E}\{\mathbf{v}\mathbf{v}^{\mathrm{H}}\} = \mathbf{\Theta}\mathbf{h}\,\mathbb{E}\{|s|^2\}\,\mathbf{h}^{\mathrm{H}}\mathbf{\Theta}^{\mathrm{H}} \in \mathbb{C}^{M\times M} \\ &= P\sigma_h^2\mathbf{\Theta}\overline{\mathbf{h}\mathbf{h}}^{\mathrm{H}}\mathbf{\Theta}^{\mathrm{H}} \in \mathbb{C}^{M\times M} \\ &\triangleq \rho\mathbf{\Theta}\overline{\mathbf{h}\mathbf{h}}^{\mathrm{H}}\mathbf{\Theta}^{\mathrm{H}} \in \mathbb{C}^{M\times M}, \end{aligned} \tag{19}$$

For notation simplicity, we denote ρ as the power of the equivalent phase-modulated signal feeding to the m-th PA as

$$\rho_m = \mathbb{E}\{|v_m|^2\} = [\mathbf{C_v}]_{m,m} = \sigma_h^2 P \triangleq \rho, \forall m. \tag{20}$$

In the following, we derive the optimal phase shift matrix $\mathbf{\Theta}^*$ that maximizes the SE, and deduce the closed-form maximum SE representation in Theorem 1.

Theorem 1: The SE in (15) can be maximized if the phase shift matrix of the TAIS $\mathbf{\Theta}^*$ satisfies

$$\mathbf{\Theta}^*\overline{\mathbf{h}} = \mathbf{a}_{\mathrm{TAIS}}(\psi_{\max}^{S_t}, \phi_{\max}^{S_t}), \tag{21}$$

where $\psi_{\max}^{S_t}$ and $\phi_{\max}^{S_t}$ are the azimuth and elevation angles of departure of the TAIS corresponding to the path with the largest small-scale fading gain in the outdoor channel matrix $\mathbf{F}$. In other words, the optimal phase shift of the m-th element of the TAIS ϑ_m^* satisfies

$$\vartheta_m^* = \angle\{\mathbf{a}_{\mathrm{TAIS}}(\psi_{\max}^{S_t}, \phi_{\max}^{S_t})\}_m - \angle\overline{h}_m, \tag{22}$$

where $\angle\{\mathbf{a}_{\mathrm{TAIS}}(\psi_{\max}^{S_t},\phi_{\max}^{S_t})\}_m$ *and* $\angle\overline{h}_m$ *denote the angle of the* m*-th element of transmit steering vector* $\mathbf{a}_{\mathrm{TAIS}}(\psi_{\max}^{S_t},\phi_{\max}^{S_t})$ *and the channel* $\overline{\mathbf{h}}$ *in (18), respectively. Then, the maximum of the SE is achieved as*

$$\overline{SE}=\left[\log_2\left|\mathbf{I}_N+\rho\overline{\gamma_s}(\rho)(N_0\mathbf{I}_N+\rho\overline{\gamma_e}(\rho)\overline{\mathbf{F}}\overline{\mathbf{F}}^{\mathrm{H}})^{-1}\overline{\mathbf{F}}\overline{\mathbf{F}}^{\mathrm{H}}\right|\right], \tag{23}$$

where $\overline{\mathbf{F}}=\mathbf{F}\mathbf{a}_{\mathrm{TAIS}}(\psi_{\max}^{S_t},\phi_{\max}^{S_t})\in\mathbb{C}^{N\times 1}$*;* $\overline{\gamma}_s(\rho)$ *and* $\overline{\gamma}_e(\rho)$ *represent the linear and nonlinear power gains, respectively, and can be given by*

$$\overline{\gamma}_s(\rho)\triangleq|\overline{g}(\rho)|^2=\left|\sum_{k=0}^{K}\beta_{2k+1}(k+1)!\rho^k\right|^2, \tag{24}$$

$$\overline{\gamma}_e(\rho)\triangleq\sum_{k=1}^{K}|\gamma_k(\rho)|^2\rho^{2k}. \tag{25}$$

Proof: See Appendix C. □

As revealed in Theorem 1, $\overline{SE}$ only depends on the transmit power of the UE, if the optimal phase shift matrix $\mathbf{\Theta}^*$ is adopted at the TAIS. In this sense, the per-element unit modulus constraint can be removed. Hence, the maximum SE can be achieved by optimizing the transmit power of the UE in one-dimension. Problem $\mathcal{P}_0$ can be simplified as

$$\begin{aligned}\mathcal{P}_1:\max_{\rho}\quad&\overline{SE}(\rho)\\ \text{s.t.}\quad&0\le\rho\le\sigma_h^2P_{\max}.\end{aligned} \tag{26}$$

Although the complexity for obtaining an optimal solution to maximize the SE in Problem $\mathcal{P}_0$ has been reduced based on Theorem 1, the Problem $\mathcal{P}_1$ is still challenging to solvepo due to the non-convexity of the SE function. In the following, we propose a low-complexity DC-based method to obtain the solution of Problem $\mathcal{P}_1$. The key idea is to equivalently transform the optimization $\mathcal{P}_1$. The objective function after transformation is shown as the difference of the two convex functions. The new problem can be then iteratively solved by using DC programming [38].

First, $\mathcal{P}_1$ can be equivalently transformed to

$$\begin{aligned}\mathcal{P}_2:\max_{\rho}\quad&\underbrace{\log_2\left(N_0+\rho(\overline{\gamma_s}(\rho)+\overline{\gamma_e}(\rho))\overline{\mathbf{F}}^{\mathrm{H}}\overline{\mathbf{F}}\right)}_{y_1(\rho)}\\&-\underbrace{\log_2\left(N_0+\rho\overline{\gamma_e}(\rho)\overline{\mathbf{F}}^{\mathrm{H}}\overline{\mathbf{F}}\right)}_{y_2(\rho)}\\ \text{s.t.}\quad&0\le\rho\le\sigma_h^2P_{\max}.\end{aligned} \tag{27}$$

(28)

Proof: The objective function of $\mathcal{P}_1$ can be rewritten as

$$\overline{SE}(\rho)=\log_2\left|\mathbf{I}_N+\rho\overline{\gamma_s}(\rho)(N_0\mathbf{I}_N+\rho\overline{\gamma_e}(\rho)\overline{\mathbf{F}}\overline{\mathbf{F}}^{\mathrm{H}})^{-1}\overline{\mathbf{F}}\overline{\mathbf{F}}^{\mathrm{H}}\right| \tag{29a}$$

$$=\log_2\left|\rho\overline{\gamma_s}(\rho)\overline{\mathbf{F}}\overline{\mathbf{F}}^{\mathrm{H}}+(N_0\mathbf{I}_N+\rho\overline{\gamma_e}(\rho)\overline{\mathbf{F}}\overline{\mathbf{F}}^{\mathrm{H}})\right|-\log_2\left|N_0\mathbf{I}_N+\rho\overline{\gamma_e}(\rho)\overline{\mathbf{F}}\overline{\mathbf{F}}^{\mathrm{H}}\right| \tag{29b}$$

$$=\log_2\left(N_0+\rho(\overline{\gamma_s}(\rho)+\overline{\gamma_e}(\rho))\overline{\mathbf{F}}^{\mathrm{H}}\overline{\mathbf{F}}\right)-\log_2\left(N_0+\rho\overline{\gamma_e}(\rho)\overline{\mathbf{F}}^{\mathrm{H}}\overline{\mathbf{F}}\right), \tag{29c}$$

where (29b) is by $\log_2\left|\mathbf{I}_N+\mathbf{A}\mathbf{B}^{-1}\right|=\log_2|\mathbf{A}+\mathbf{B}|-\log_2|\mathbf{B}|$; (29c) is by the Weinstein–Aronszajn identity $|\mathbf{I}_N+\mathbf{A}\mathbf{B}|=|\mathbf{I}_M+\mathbf{B}\mathbf{A}|$. □

Note that the objective function of Problem $\mathcal{P}_2$ can be viewed as a difference of two convex functions, denoted by $y_1(\rho)-y_2(\rho)$, and the feasible set of Problem $\mathcal{P}_2$ is convex. Now, we can solve Problem $\mathcal{P}_2$ by using DC programming. The main idea is to iteratively solve convex approximations of Problem $\mathcal{P}_2$, which is obtained by linearizing the function $y_2(\rho)$:

$$y_2(\rho)=\log_2\left(N_0+\rho\overline{\gamma_e}(\rho)\overline{\mathbf{F}}^{\mathrm{H}}\overline{\mathbf{F}}\right). \tag{30}$$

Specifically, the convex approximation of Problem $\mathcal{P}_2$ at the i-th iteration is given below:

$$\begin{aligned}\mathcal{P}_3:\rho^{(i)}\triangleq\arg\max_{\rho}\quad&y_1(\rho)-\hat{y_2}(\rho,\rho^{(i-1)})\\ \text{s.t.}\quad&0\le\rho\le\sigma_h^2P_{\max},\end{aligned} \tag{31}$$

where

$$\hat{y_2}(\rho,\rho^{(i-1)})=y_2(\rho^{(i-1)})+y_2'(\rho^{(i-1)})(\rho-\rho^{(i-1)}), \tag{32}$$

and $y_2'(\rho)$ is the derivative of the distortion power function and can be written as

$$y_2'(\rho)=\frac{1}{y_2(\rho)\ln 2}\overline{\mathbf{F}}^{\mathrm{H}}\overline{\mathbf{F}}\left(\overline{\gamma_e}(\rho)+\rho\overline{\gamma_e}'(\rho)\right). \tag{33}$$

$\overline{\gamma_e}'(\rho)$ denotes the derivative of the nonlinear power gain, as given by

$$\overline{\gamma_e}'(\rho)=\sum_{k=1}^{K}\left(2k|\gamma_k(\rho)|^2\rho^{2k-1}+|\gamma_k(\rho)|\rho^{2k}\frac{\mathrm{d}\gamma_k(\rho)}{\mathrm{d}\rho}\right), \tag{34}$$

with

$$\frac{\mathrm{d}\gamma_k(\rho)}{\mathrm{d}\rho}=\sqrt{\frac{1}{k+1}}\sum_{q=k+1}^{K}\beta_{2k+1}\binom{q}{k}(q+1)!\,(q-k)\rho^{(q-k-1)}. \tag{35}$$

Problem $\mathcal{P}_3$ is a convex optimization problem and can be solved using standard convex optimization techniques, e.g., the CVX tools.

The lower bound of $\overline{SE}$ is given in Corollary 1.

Corollary 1: A lower-bound of SE is described as follows:

$$\overline{SE}\ge\log_2\left(1+\frac{\overline{\gamma}_s(\rho)}{\overline{\gamma}_e(\rho)+\frac{N_0}{\kappa\rho}}\right). \tag{36}$$

where $\kappa=\left|\left(\mathbf{a}_{\mathrm{BS}}^{\mathrm{H}}(\psi_{\max}^{B},\phi_{\max}^{B})\mathbf{F}\mathbf{a}_{\mathrm{TAIS}}(\psi_{\max}^{S_t},\phi_{\max}^{S_t})\right)\right|^2$ *is the effective channel gain between the UE and the BS;* $\psi_{\max}^{B}$ *and* $\phi_{\max}^{B}$ *are the azimuth and elevation angles of arrival of the path with the largest small-scale fading gain of the outdoor channel matrix* $\mathbf{F}$*. This bound is tight if* $L=1$.

Proof: See Appendix D. □

Corollary 1 shows that a larger array gain κ can be achieved as the increase of the number of TAIS elements M, indicating the proportional increase of the SE with the number of TAIS elements.

We present the power consumption models for the proposed TAIS system and the passive RIS design, and analyze and compare their energy efficiency. The main power-consuming elements are transmitter (UE), receiver (BS), amplifiers, and RIS elements. To this end, we first introduce the power efficiency of the PA, as defined in [33]:

$$\eta \triangleq \frac{\rho_{\text{out}}}{\rho_{\text{cons}}}, \tag{37}$$

where $\rho_{\text{out}} = \rho\big(\overline{\gamma_s}(\rho) + \overline{\gamma_e}(\rho)\big)$ is the radiated power from the PA, including both the signal and distortion power, and ρ_{cons} is the power consumed by the PA, including both the radiated and dissipated power. The power consumed by the PA can be expressed as [39]

$$\rho_{\text{cons}} = \frac{\sqrt{\rho_{\max}}}{\eta_{\max}}\sqrt{\rho_{\text{out}}} = \frac{\sqrt{\rho_{\max}}}{\eta_{\max}}\sqrt{\rho\big(\overline{\gamma_s}(\rho) + \overline{\gamma_e}(\rho)\big)}, \tag{38}$$

where $\rho_{\max}$ is the maximum output power, and $\eta_{\max}$ is the maximum efficiency of the PA. The power consumption of all PAs is given by

$$\overline{P}_{\text{amp}} = M\frac{\sqrt{\rho_{\max}}}{\eta_{\max}}\sqrt{\rho\big(\overline{\gamma_s}(\rho) + \overline{\gamma_e}(\rho)\big)}. \tag{39}$$

The phase shift of each RIS element is arranged by programmable electronic circuits that consume power as well. The power consumption of the RIS depends on the phase resolution of RIS elements and is modeled as

$$P_{\text{RIS}} = MP_{\text{PS}}, \tag{40}$$

where P_{PS} is the power consumption of a RIS element. We consider a 6-bit phase resolution for each RIS element, which could consume 7.8 mW power according to [40]. The total power consumption of the proposed TAIS system is expressed as follows:

$$P_{\text{tot}}^{\text{TAIS}} = \mu P + P_{\text{Tx}} + P_{\text{Rx}} + MP_{\text{PS}} + \overline{P}_{\text{amp}}, \tag{41}$$

where $\mu = \eta_{\text{ue,max}}^{-1}$ and $\eta_{\text{ue,max}}$ denotes the maximum power efficiency of the UE. P_{Tx} and P_{Rx} are the hardware dissipated static powers at Tx (UE) and Rx (BS), respectively. Therefore, they are constant and do not depend on the system parameters. Likewise, by only omitting the power consumed by the PA between the RISs, the power consumption of the passive RIS-assisted system is written as follows:

$$P_{\text{tot}}^{\text{RIS}} = \mu P + P_{\text{Tx}} + P_{\text{Rx}} + MP_{\text{PS}}. \tag{42}$$

We define energy efficiency as the energy consumption for one information bit transmitted from the UE to the BS (in bits/Joule), as follows [41]

$$\xi_{\text{EE}} = \frac{BW \times SE^i}{P_{\text{tot}}^i}, \tag{43}$$

where BW is the communication bandwidth. SE^i and P_{tot}^i represent SE and the total power consumed by the system where $i \in \{\text{TAIS}, \text{RIS}\}$, respectively. The spectral efficiency of TAIS, SE^{TAIS}, is analyzed in Section III and can be obtained by using (15). The spectral efficiency of RIS is given by

$$SE^{\text{RIS}} = \log_2\left[\det\left(\mathbf{I}_N + \frac{P}{N_0}\mathbf{F}\boldsymbol{\Theta}\mathbf{h}\mathbf{h}^{\text{H}}\boldsymbol{\Theta}^{\text{H}}\mathbf{F}^{\text{H}}\right)\right], \tag{44}$$

V. Asymptotic Performance Analysis of Spectral Efficiency

In this section, we investigate the asymptotic spectral efficiency of uplink transmission in the TAIS-enhanced indoor-to-outdoor communications. The power scaling law with an infinitely large number of elements under both the sparse and rich scattering channel models are analyzed. The result accurately captures the impact of the PA's nonlinearity and the channel parameters on the spectral efficiency.

A. Approximation Analysis of Nonlinearity

We first present the asymptotic spectral efficiency analysis under different transmit power levels, as stated in Theorem 2.

Theorem 2: For a finite number of TAIS elements, when the indoor signal-to-noise ratio (SNR) is high, and the average power of TAIS's incidence signal goes infinite, the SE approaches to

$$\lim_{\rho\to\infty}\overline{SE} = \log_2\left(1 + \frac{\left[\beta_{2K+1}(K+1)!\right]^2}{\sum_{k=1}^{K}\frac{1}{k+1}\left[\beta_{2k+1}\binom{K}{k}(K+1)!\right]^2}\right). \tag{45}$$

When the average power of the incidence signal of the TAIS goes to 0, the SE approaches to

$$\lim_{\rho\to 0}\overline{SE} = \beta_1^2\frac{\rho\kappa}{N_0\ln 2} \tag{46}$$

Proof: When the power ρ approaches ∞ at the TAIS, the linear and nonlinear gains in (24) and (25) approach to

$$\lim_{\rho\to\infty}\overline{\gamma}_s(\rho) = \left[\beta_{2K+1}(K+1)!\right]^2\rho^{2K}, \tag{47}$$

$$\lim_{\rho\to\infty}\overline{\gamma}_e(\rho) = \sum_{k=1}^{K}\frac{1}{k+1}\left[\beta_{2k+1}\binom{K}{k}(K+1)!\right]^2\rho^{2K}. \tag{48}$$

With asymptotic linear and nonlinear power gains in (47) and (48), the lower-bound of the SE in (36) approaches to

$$\begin{aligned}\lim_{P\to\infty}\overline{SE} &= \lim_{\rho\to\infty}\log_2\left(1 + \frac{\overline{\gamma}_s(\rho)}{\overline{\gamma}_e(\rho) + \frac{N_0^2}{\rho\kappa}}\right)\\ &= \log_2\left(1 + \frac{\left[\beta_{2K+1}(K+1)!\right]^2}{\sum_{k=1}^{K}\frac{1}{k+1}\left[\beta_{2k+1}\binom{K}{k}(K+1)!\right]^2}\right)\end{aligned} \tag{49}$$

In the low SNR regime, the power $\rho \to 0$ at TAIS, the lower-bound of the SE approaches to

$$\lim_{P\to 0}\overline{SE} = \beta_1^2\frac{\rho\kappa}{N_0\ln 2} \propto \beta_1^2\frac{PM^2N}{N_0\ln 2} \tag{50}$$

which is obtained by using $\ln(1+x) \sim x$. □

Remark: Theorem 2 shows that the TAIS can enhance the SE of uplink transmission in indoor-to-outdoor communication, especially in the low SNR region. In this case, the SE increases with both the number of elements M at the TAIS and the transmit power P of the UE. However, different from the observations in most active RIS work such

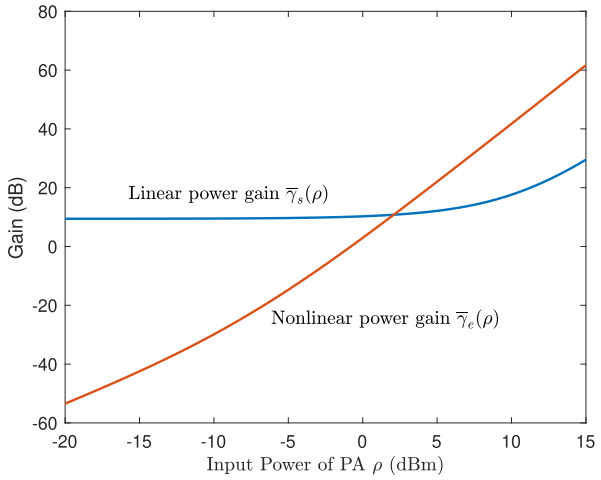

Fig. 3. Linear and nonlinear gains of the power amplifier.

as [17], [18], and [27], the increase of transmit power cannot always lead to a higher SE due to the nonlinear amplification. In particular, as ρ increases, the power amplification enters into a saturation region, where the nonlinear power gain $\overline{\gamma}_e$ increases and dominates the SE performance. The linear and nonlinear power gains as a function of the input power ρ are plotted in Fig. 3. The distortion increases rapidly and degrades the SE performance, which necessitates the optimal power control ρ. The optimal input power ρ that maximizes SE can be obtained by using the method stated in Section IV.

The maximum spectral efficiency of direct indoor-to-outdoor transmission is given by

$$\overline{SE}^{\text{Direct}} = \log_2\left[\left(1+\frac{P\|\mathbf{h}_D\|^2}{N_0}\right)\right], \tag{51}$$

where $\mathbf{h}_D \in \mathbb{C}^{N\times 1}$ represent the channel between UE and BS, denoted by $\mathbf{h}_D \in \mathbb{C}^{N\times 1}$. The maximum spectral efficiency is achieved by using maximum ratio combining at BS, i.e., $\mathbf{w}_{\text{BS}} = \mathbf{h}_D^{\text{H}}/\|\mathbf{h}_D\|$. In the low SNR regime, the transmit power $P \to 0$ at UE, the lower-bound of the SE of typical approaches to

$$\lim_{P\to 0} \overline{SE}^{\text{Direct}} = \frac{P\|\mathbf{h}_D\|^2}{N_0 \ln 2} \propto \frac{PN}{N_0 \ln 2}. \tag{52}$$

By comparing with (50), the proposed TAIS can achieve a higher SE by the following:

- *Amplification Gain:* The TAIS achieves higher SE through the amplification process, which is proportional to the amplification gain $M\beta_1^2 > 1$.
- *Beamforming Gain:* The TAIS can achieve a larger effective beamforming gain by optimizing its phase shift matrix. The effective channel gain achieved by TAIS κ is proportional to both the element number M at TAIS and the antenna number N at BS.

B. Power Scaling Law With Infinitely Large Number of Elements M

Now we characterize the scaling law of the SE performance with respect to the number of the reflecting elements M. The asymptotic SE performance of the TAIS-enhanced communication with an infinite number of elements is analyzed under both the sparse and rich scattering channel models.

1) Sparse Channel Analysis: For the sparse channel considered in Section II-D, when the number of elements M goes to infinite, $M \to \infty$, the SE approaches to

$$\begin{aligned}\lim_{M\to\infty} \overline{SE} &= \lim_{M\to\infty} \log_2\left(1+\frac{\overline{\gamma}_s(\rho)}{\overline{\gamma}_e(\rho)+\frac{N_0}{\rho\kappa}}\right)\\ &= \lim_{M\to\infty} \log_2\left(1+\frac{\overline{\gamma}_s(\rho)}{\overline{\gamma}_e(\rho)}\right)\end{aligned} \tag{53}$$

where the equality is by the fact that the effective channel gain between the UE and the BS κ goes to infinite when $M \to \infty$. When the power of the incidence signal of the TAIS goes to infinite and 0, the SE approaches to (45) and (46), respectively, as presented in Theorem 2. When the PAs work in the linear region, we have

$$\lim_{M\to\infty} \overline{SE} = \lim_{M\to\infty} \log_2\left(1+\overline{\gamma}_s(\rho)\right) \tag{54}$$

2) Rich-Scattering Channel Analysis: We characterize the scaling law under the rich-scattering Rayleigh channel and optimal receive combiner for a single UE data stream. We first redefine the BS-TAIS channel matrix as $\mathbf{F} \in \mathbb{C}^{N\times M}$ and the TAIS-user channel vector $\mathbf{h} \in \mathbb{C}^{M\times 1}$, respectively. Based on the assumption of the Rayleigh channel model, $\mathbf{h} \sim \mathcal{CN}(\mathbf{0}_M, \varrho_h^2\mathbf{I}_M)$ and $\mathbf{F} \sim \mathcal{CN}(\mathbf{0}_{N\times M}, \varrho_f^2\mathbf{I}_{N\times M})$.

With (25), we have signal-to-noise and distortion ratio (SNDR) as

$$\text{SNDR} = \frac{\rho\overline{\gamma_s}(\rho)|\mathbf{w}^{\text{H}}\mathbf{F}\boldsymbol{\Theta}\mathbf{h}|^2}{\rho\overline{\gamma_e}(\rho)|\mathbf{w}^{\text{H}}\mathbf{F}\boldsymbol{\Theta}\mathbf{h}|^2+N_0}. \tag{55}$$

The singular value decomposition of channel matrix $\mathbf{F}$ is given by $\mathbf{F} = \mathbf{U}\boldsymbol{\Sigma}\mathbf{V}^{\text{H}}$. Denote $\mathbf{u}_{\max}$ and $\boldsymbol{\nu}_{\max}$ as the left and right singular vectors corresponding to the maximum singular value of $\mathbf{F}$. The SNDR in (55) is maximized when the optimal combiner $\mathbf{w}^* = \mathbf{u}_{\max}$ and optimal phase shift matrix satisfies $\boldsymbol{\Theta}^*\mathbf{h}/\|\mathbf{h}\| = \boldsymbol{\nu}_{\max}$, i.e. the optimal phase shift of the m-th element satisfies

$$\theta_m^* = \angle\nu_{\max,m} - \angle h_m, \tag{56}$$

where $\angle\nu_{\max,m}$ and $\angle h_m$ denote the angle of the m-th element of singular vector $\boldsymbol{\nu}_{\max}$ and the TAIS-user channel vector $\mathbf{h}$, respectively. Let $\overline{\mathbf{H}} = \mathbf{F}\boldsymbol{\Theta}^*\mathbf{h} \in \mathbb{C}^{N\times 1}$ denote the end-to-end channel between the UE and BS when the optimal phase shift matrix $\boldsymbol{\Theta}^*$ is adopted. The only non-zero singular value of the end-to-end channel $\overline{\mathbf{H}}$ is given by $\lambda_{\overline{\mathbf{H}}} = \text{Tr}(\overline{\mathbf{H}}\overline{\mathbf{H}}^{\text{H}}) = \left|\sum_{n=1}^{N}\sum_{m=1}^{M}|F_{n,m}|\,|h_m|\right|^2$. Thus, when the optimal combiner $\mathbf{w}^*$ and optimal phase shift in (56) are applied, the maximum SNDR is achieved as follows

$$\begin{aligned}\text{SNDR} &= \frac{\rho\overline{\gamma_s}(\rho)|\mathbf{w}^{*\text{H}}\mathbf{F}\boldsymbol{\Theta}^*\mathbf{h}|^2}{\rho\overline{\gamma_e}(\rho)|\mathbf{w}^{*\text{H}}\mathbf{F}\boldsymbol{\Theta}^*\mathbf{h}|^2+N_0}\\ &= \frac{\rho\overline{\gamma_s}(\rho)\left|\sum_{n=1}^{N}\sum_{m=1}^{M}|F_{n,m}|\,|h_m|\right|^2}{\rho\overline{\gamma_e}(\rho)\left|\sum_{n=1}^{N}\sum_{m=1}^{M}|F_{n,m}|\,|h_m|\right|^2+N_0}.\end{aligned} \tag{57}$$

By letting $M \to \infty$, according to the law of large numbers, we have

$$\sum_{n=1}^{N}\sum_{m=1}^{M}|F_{n,m}|\,|h_m| \to MN\frac{\pi\varrho_h\varrho_f}{4} \triangleq \delta. \tag{58}$$

Since $|F_{n,m}|$ and $|h_m|$ are statistically independent and follow Rayleigh distribution with mean values $\sqrt{\pi}\varrho_f/2$ and $\sqrt{\pi}\varrho_h/2$, respectively. As a result, when $M \to \infty$ the asymptotic SNDR of the considered system is given by

$$\text{SNDR} \to \frac{\frac{\rho M^2N^2\pi^2\varrho_h^2\varrho_f^2}{16}\overline{\gamma_s}(\rho)}{\frac{\rho M^2N^2\pi^2\varrho_h^2\varrho_f^2}{16}\overline{\gamma_e}(\rho)+N_0} = \frac{\overline{\gamma_s}(\rho)}{\overline{\gamma_e}(\rho)+N_0/\delta^2}, \tag{59}$$

where $\delta^2 = \frac{\rho M^2N^2\pi^2\varrho_h^2\varrho_f^2}{16}$.

In the following, we further analyze the asymptotic SNDR under different PA working conditions. (a)

1) When PAs work in the linear region, we have

$$\text{SNDR} \to \frac{\rho M^2N^2\pi^2\varrho_h^2\varrho_f^2}{16N_0}\overline{\gamma_s}(\rho). \tag{60}$$

In other words, the SNDR is dominated by the SNR when the PAs work in the linear region; the nonlinear distortion is negligible compared to noise. It is similar to the results shown in [18], where linear amplification is assumed. The SE approaches to

$$\lim_{M\to\infty}\overline{SE} \to \log_2\left(1+\frac{\rho M^2N^2\pi^2\varrho_h^2\varrho_f^2}{16N_0}\overline{\gamma_s}(\rho)\right). \tag{61}$$

2) When PAs are heavily saturated, SNDR $\to \frac{\overline{\gamma_s}(\rho)}{\overline{\gamma_e}(\rho)}$ and SE approaches to

$$\begin{aligned}&\lim_{M\to\infty}\lim_{\rho\to\infty}\overline{SE}\\ &= \lim_{\rho\to\infty}\log_2\left(1+\frac{\overline{\gamma}_s(\rho)}{\overline{\gamma}_e(\rho)}\right)\\ &= \log_2\left(1+\frac{[\beta_{2K+1}(K+1)!]^2}{\sum_{k=1}^{K}\frac{1}{k+1}\left[\beta_{2k+1}\binom{K}{k}(K+1)!\right]^2}\right).\end{aligned} \tag{62}$$

It is observed that, when the PAs are heavily saturated, the SE is independent of the number of elements M. The SE cannot always benefit from the increase of the element number M or the number of the receiving antennas N.

3) In the low SNR region, i.e., the input power ρ approaches to 0, we have

$$\lim_{M\to\infty}\lim_{\rho\to 0}\overline{SE} = \beta_1^2\frac{\delta^2}{N_0\ln 2} = \beta_1^2\frac{\rho M^2N^2\pi^2\varrho_h^2\varrho_f^2}{16N_0\ln 2}, \tag{63}$$

which is achieved by using $\ln(1+x)\sim x$.

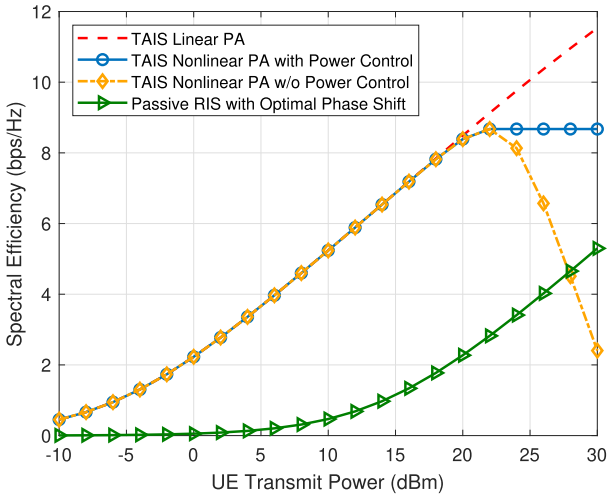

Fig. 4. Spectral efficiency under different UE transmit power P: $M=100$, $d_1 = 2.5$ m, $d_2=45$ m.

VI. Performance Evaluation

In this section, we evaluate the performance of the proposed TAIS-enhanced indoor-to-outdoor communication system in simulations. We simulate a system operating at $f_c = 28$ GHz. The number of antennas at the BS and the number of elements at TAIS are configured as $N = 10$ and $M = 100$ unless specified otherwise. For the mmWave channels, we set the number of paths as $L_1 = L_2 = 10$; the azimuth and elevation angles of arrival and departure are randomly generated according to the Laplacian distribution with an angle spread of 10°; the complex gain follows the complex Gaussian distribution $\mathcal{CN}(0, 10^{-0.1\,PL_i(d)})$, $i \in \{1,2\}$. The noise power is configured as $N_0 = -105$ dBm. Referring the path loss models for NLOS cases in the indoor (InH) environment, i.e., $PL_1(d_1)$, and outdoor (UMi) environment, i.e., $PL_2(d_2)$, are given as follows, respectively [7]:

$$PL_1(d_1)[\text{dB}] = 43.3\log_{10}(d_1) + 11.5 + 20\log_{10}(f_c), \tag{64}$$

$$PL_2(d_2)[\text{dB}] = 36.7\log_{10}(d_2) + 22.7 + 26\log_{10}(f_c), \tag{65}$$

where d_1 and d_2 are the distances between the TAIS and the UE and the BS, respectively. As for the amplification process in TAIS, the parameters of the PA model: $\beta_1 = 2.96$, $\beta_3 = 448.41e^{-\jmath 2.816}$ and $\beta_5 = 3000e^{\jmath 0.39}$ [41], [42]. $\mu = 1.2$, $\eta_{\max} = 0.55$, $\rho_{\max}$=30 dBm, $P_{\text{Rx}} = 9$ dBW, $P_{\text{Tx}} = 10$ dBm, $P_{\text{PS}} = 7.8$ mW [39], [40], [41], [42], [43].

We repeat the simulations 2,000 times with independent channel realizations each time, and the simulation results are averaged. For comparison, we also evaluate the passive RIS with optimal phase shift matrix $\boldsymbol{\Theta}^*$. For a fair comparison, for the benchmark with passive RIS, we assume that an extra amplification gain is added at the BS and is equal to 35 dB. We also evaluate the performance under an ideally linear power amplification assumption, which gives a high performance bound but is hard to achieve in reality.

A. Performance Comparison

Fig. 4 plots the spectral efficiency when the UE transmits with different power budget P. The distance from TAIS to UE

and BS are $d_1 = 2.5$ m and $d_2 = 45$ m, respectively. We can observe the proposed TAIS outperforms the passive RIS system with the same transmit power of the UE, by optimal power and phase shifts optimization at TAIS. The passive RIS with optimal phase shift can achieve the maximum channel gain by beamforming. The huge path loss causes the weak direct link from indoor to outdoor, resulting in a low uplink transmission SE for the case of passive RIS in indoor-to-outdoor communications. The passive RIS also only achieves negligible gain in SE due to the weak direct link in indoor-to-outdoor communications. For example, to achieve the same $SE = 5$ bps/Hz, the TAIS can save 20 dBm transmit power of UE compared to the passive RIS with optimal phase shifts. Notice that UEs are powered by a battery with limited capacity and need to be recharged after the battery drains, while the TAIS is powered by the regular power supply (mains). In this sense, energy-saving for UE is more critical to the system.

Another observation from Fig. 4 is that the SE is a non-monotonically increasing function of the input power due to the presence of nonlinear distortion. The SE increases with the transmit power of the UE when $P < 20$ dBm, where the amplification is in the linear region. The distortion is negligible compared to the noise power received at the BS. However, instead of having a linear increase with input power (red dash line in Fig. 4) as shown in [18], the SE degrades when $P > 20$ dBm. The reason is that the SE decreases with the increase of transmit power when the distortion dominates the SE performance. To this end, the UE's transmit power needs to be meticulously optimized to avoid distortion and maximize the SE.

Fig. 5 plots the spectral efficiency versus the transmit power budget P when the UE locates 3 m and 5 m away from the TAIS, respectively. The proposed TAIS can obtain a maximum uplink SE of 8.7 bps/Hz when $d_1 = 3$ m, achieving 24.7% increase of SE compared to the case with passive RIS with optimal phase shift. As observed in Fig. 5, standing away from the TAIS, e.g., $d_2 = 5$ m, lowers the UE's SE since a larger indoor path loss incurs. It is also observed that the optimal UE transmit power for TAIS depends on the distance or path loss between the UE and TAIS, i.e., indoor distance d_1. Larger input power is needed to compensate for the path loss to achieve the same power level at the TAIS. On the contrary, when the UE is close to the TAIS, and the indoor path loss is small, the power of the incidence signal on TAIS increases, which can push PAs into a deeper saturation regime. In this way, more distortion is generated due to PA saturation and thus degrades the performance, e.g., indoor distance $d_1 = 3$ m. Therefore, it is necessary to jointly optimize the transmit power of UE and the phase shift matrix at TAIS to maximize the SE.

We further evaluate the spectral efficiency when the UE is located at difference indoor distances (d_1) to the TAIS. The results are shown in Fig. 6. It is observed that SE decreases with d_1 due to path loss. In particular, the SE of TAIS is lower than the passive RIS when the UE's indoor distance is small. In this case, the power of the incidence signal on the TAIS is large and distorts the signal during the amplification process, even with optimal power control at the TAIS. Without power control at the TAIS, SE decreases rapidly since the distortion grows larger and degrades the performance when UE is closer

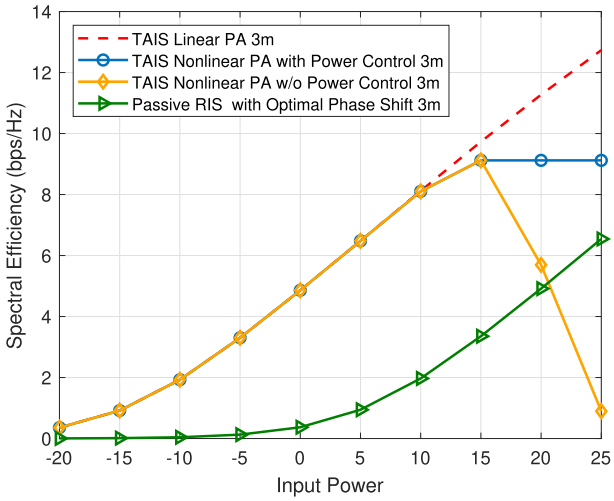

(a) Indoor distance $d_1 = 3$ m

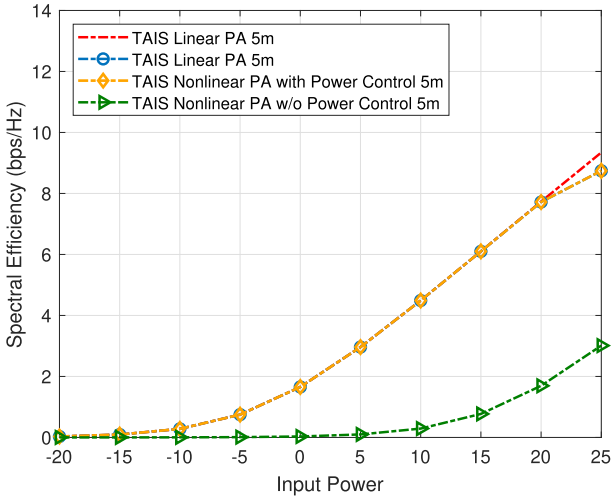

(b) Indoor distance $d_1 = 5$ m

Fig. 5. Spectral efficiency under different positions of UE with different transmit power P: $M = 100$, $d_2 = 45$ m.

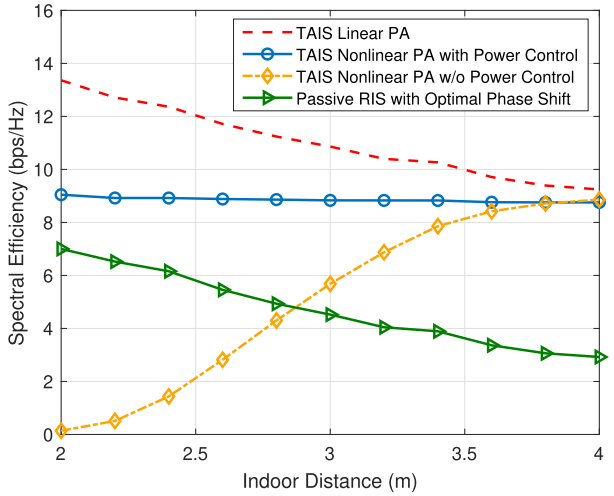

Fig. 6. Spectral efficiency under different distance between UE and TAIS d_1: $M = 100$, $d_2 = 45$ m, $P = 20$ dBm.

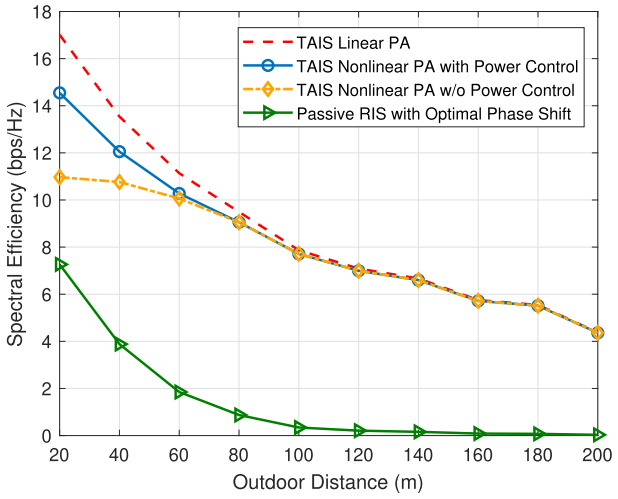

Fig. 7. Spectral efficiency under different distance between BS and TAIS d_2: $M = 100$, $d_1 = 2.5$ m, $P = 20$ dBm.

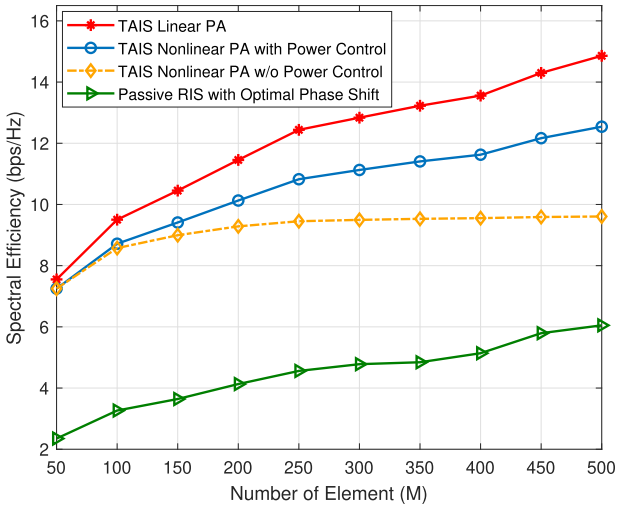

Fig. 8. Spectral efficiency versus number of elements on TAIS M: $P = 22$ dBm, $d_1 = 2.5$ m, $d_2 = 45$ m.

to the TAIS. As observed, when the UE is far from the TAIS ($d = 5$ m), the power level of the incidence signal is lower than the saturation point of the PAs, which exhibits a similar SE performance regardless of power control.

Fig. 7 plots the spectral efficiency under different outdoor distance d_2 to the BS. It is observed that SE is low when the BS is far from the building (or TAIS) due to the huge path loss incurred when the mmWave signal propagates through the outdoor environment. It is also confirmed that the TAIS and the RIS should be deployed either close to UE or BS due to the product effect of the outdoor and indoor channels, as shown in [18]. The proposed TAIS can achieve higher SE by amplifying the signal with a larger beamforming gain. In particular, by jointly optimizing the input power and phase shift at TAIS, 32.6% SE improvement can be achieved when $d_2 = 20$ m, compared with the passive RIS system. Another observation is that when the building (i.e., TAIS) is far from the BS, e.g., $d_2 > 100$ m, the power control has a negligible impact on the SE performance since the power level of the incidence signal is low, and the PAs of the TAIS have not been heavily saturated.

Fig. 8 plots the spectral efficiency versus the number of elements M on the TAIS (or passive RIS). The SE of both TAIS and RIS improves as the number of elements M increases. It is because a larger channel gain can be achieved with an optimal phase shift matrix applied at either TAIS or passive RIS, which is proportional to the number of elements M. In addition to larger channel gain, the TAIS achieves higher SE due to the signal amplification. We also observe that the SE of the TAIS degrades when power control at UE is not adopted. The distortion increases and degrades the SE performance when the power control is not considered.

Fig. 9 plots the power consumption versus the number of elements at the proposed TAIS system and passive RIS. It is observed that both the power consumption of TAIS and passive RIS increases with the number of elements, since more energy is consumed by a larger number of phase shifters. TAIS enhances indoor-to-outdoor communications by refracting and amplifying the incident signal, which is bound to increase total

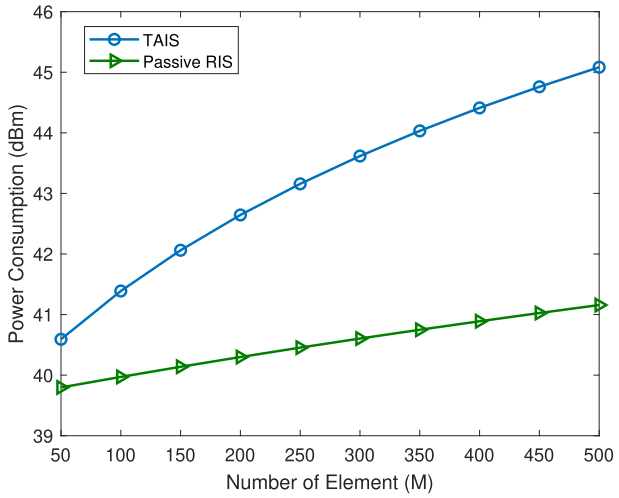

Fig. 9. Power consumption versus the number of elements M on TAIS and passive RIS: $P = 22$ dBm, $d_1 = 2.5$ m, $d_2 = 45$ m.

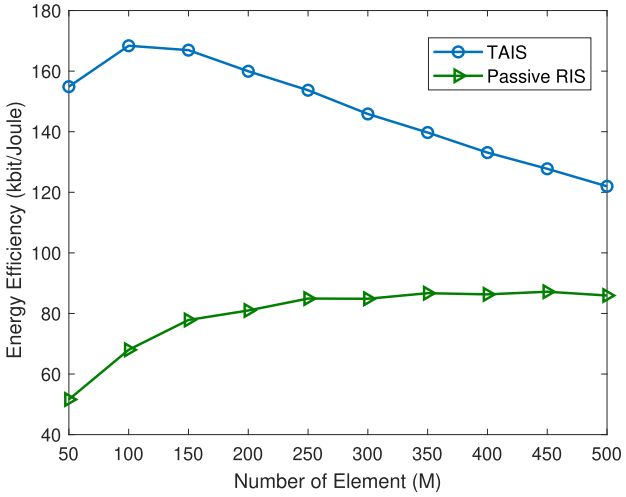

Fig. 10. Energy efficiency versus number of elements M on TAIS and passive RIS: $P = 22$ dBm, $d_1 = 2.5$ m, $d_2 = 45$ m, $BW = 200$ kHz.

power consumption. As observed in Fig. 10, TAIS has a higher energy efficiency, although the amplification process consumes

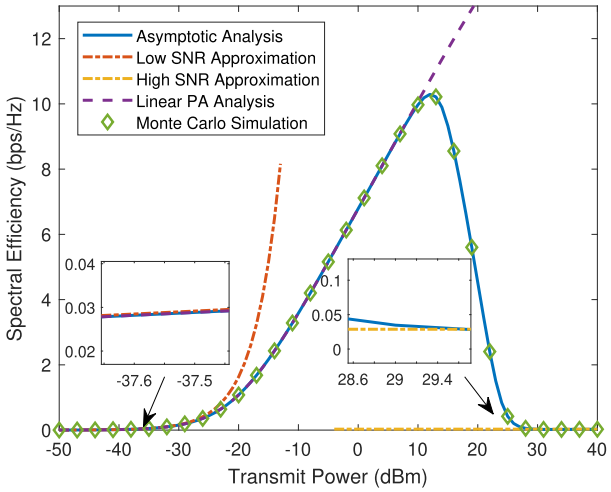

Fig. 11. Spectral efficiency versus transmit power P: $M = 200$, $N = 10$, $d_1 = 1$ m, $d_2 = 45$ m.

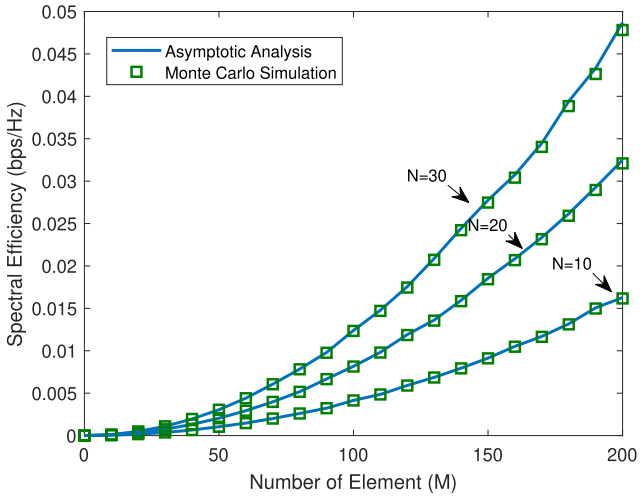

Fig. 12. Spectral efficiency in low SNR region versus different number of elements M on TAIS: $P = -40$ dBm, $d_1 = 1$ m, $d_2 = 45$ m.

more power. It is because TAIS can drastically increase the SE and utilize the energy more efficiently. On the other hand, TAIS is powered by the regular power supply (mains), which offloads the energy consumption from UE to the mains-powered TAIS and boosts the SE without challenging the battery of UE. TAIS can be in sleep mode to save energy when there is no transmission request from the UE. In this sense, the proposed TAIS could provide an energy-efficient approach to enhance indoor-to-outdoor communications. It is also observed in Fig. 10 that energy efficiency values start to decline after some points. This is because the increase in power consumption brought by more PAs is much larger than their contribution to the increase of achievable rates.

B. Asymptotic Analysis Verification

In this section, we verify the asymptotic analysis of spectral efficiency under both sparse channel and Rayleigh channel models that are previously presented in Section V.

1) Asymptotic Analysis Under Sparse Channel: Fig. 11 plots the spectral efficiency for the case with a finite element number $M = 200$ and the input power P goes to 0 and infinity, as studied in Theorem 2. The simulated curves of the asymptotic analysis, low SNR approximation, high SNR approximation, and linear approximation are obtained based on (53), (46), (45) and (54), respectively. The Monte Carlo simulated curve is obtained based on (23) by averaging the results over 2,000 random channel realizations. Our asymptotic analysis for large element M is in strong agreement with the exact Monte Carlo simulation. The tight match of low, high SNR, and linear PA approximation with the exact Monte Carlo simulation is also observed in their specified transmit power region. As mentioned in Theorem 2, the increase of transmit power cannot always lead to a higher SE due to the PA's nonlinearity amplification. Specifically, when the transmit power goes to infinity and PAs are heavily saturated, the SE is determined by the characteristics of the PAs, regardless of the increase of input power, which verifies Theorem 2.

Fig. 12 plots the spectral efficiency for the case that the number of elements $M \to \infty$, when the transmit power is

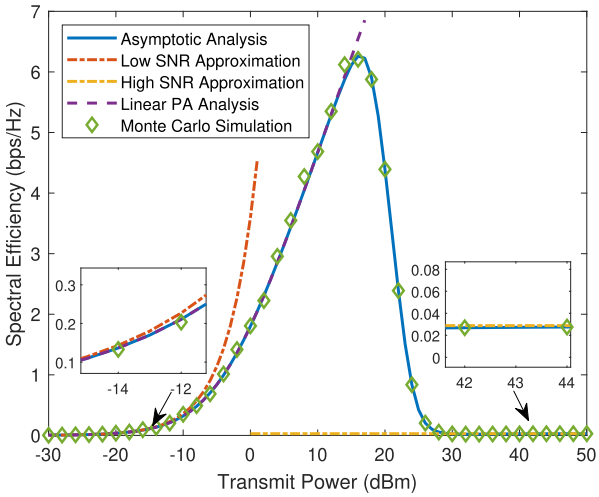

Fig. 13. Spectral efficiency versus different input power P: $M = 200$, $\varrho_h = 0.18$, $\varrho_g = 0.18$, $N = 10$.

$P = -40$ dBm (low SNR region). The simulated curves of the low SNR asymptotic analysis, and Monte Carlo simulated curves are obtained based on (46) and (23), respectively. As observed, our approximate analysis has a strong agreement with the exact Monte Carlo simulations, which verifies the power scaling law with infinitely large elements. As suggested in Section V-B.1, the SE increases with the number of receiving antennas N at BS.

2) Asymptotic Analysis Under Rayleigh Channel: Fig. 13 plots the spectral efficiency for the case that the finite element number $M = 200$ and the input power goes to 0 and infinity in Theorem 2. The number of antennas at BS $N = 10$, and Rayleigh channel model is assumed with $\varrho_h = 0.18$ and $\varrho_g = 0.18$. The simulated curves of the asymptotic analysis, low SNR approximation, high SNR approximation, and linear approximation are obtained based on (59), (63), (62) and (61), respectively. The Monte Carlo simulated curve is obtained based on (23) by averaging the results over 2,000 random channel realizations. Our asymptotic analysis for large element M strongly agrees with the exact Monte Carlo simulation.

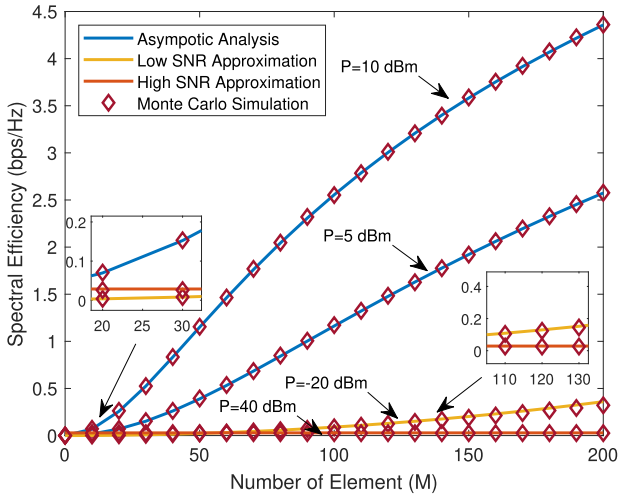

Fig. 14. Spectral efficiency versus different number of elements on TAIS M, $\varrho_h = 0.18$, $\varrho_g = 0.18$, $N = 10$.

The asymptotic analysis under low, high SNR, and linear PA approximation can also depict the performance behavior. As suggested in Section V-B.2, the SE increases with the input power until a saturation point, where the linear power gain $\overline{\gamma}_s$ dominates the performance. However, as the increase of input power, the gap between the linear power gain $\overline{\gamma}_s$ and the nonlinear power gain $\overline{\gamma}_e$ is asymptotically fixed, as shown in Fig. 3. The SE degrades significantly due to the nonlinear distortion and no longer grows with the input power.

Fig. 14 plots the spectral efficiency for the case with the number of elements $M \to \infty$. The simulated curves based on asymptotic analysis, low SNR approximation, high SNR approximation, and Monte Carlo simulated curves are obtained based on (59), (63), (62) and (23), respectively. As observed, our approximate analysis has a strong agreement with the exact Monte Carlo simulations, which verifies the power scaling law with an infinitely large number of elements M. As suggested in Section V-B.2, the SE increases with the number of elements M at TAIS and input power, when the PAs are not heavily saturated. The SE is independent of the element number M when PAs are heavily saturated. Though the SE scales with M in the low SNR regime, the increase of SE is almost invisible due to the low transmit power.

VII. Conclusion

In this paper, we proposed a novel transparent amplifying intelligent surface (TAIS) architecture for uplink enhancement in indoor-to-outdoor mmWave communication. TAIS is an optically-transparent refractor integrated with the window, and can adjust the phase shift of an impinging signal, perform beamforming and amplify the signal, thus enhancing the network service for indoor UEs. A SE maximization problem was structured by jointly optimizing the phase shift matrix of the TAIS and the transmit power of the UE. Considering PAs' nonlinearity in TAIS, we proved the optimal phase shift matrix that maximizes the spectral efficiency and deduces its closed-form representation. Based on the derived optimal phase shift matrix, the SE maximization can be transferred to the transmit power optimization problem. A power optimization algorithm was established based on the DC programming, with significantly low complexity. Extensive simulations demonstrated that our approach can boost the uplink capacity with efficient energy saving of indoor UEs. In this paper, we neglect penetration loss for both TAIS and RIS systems. However, we recognize the significance of progressing beyond idealized scenarios. Future work should consider more nuanced models that factor in material losses, deviations from normal incidence, and other real-world complexities.

Appendix A
Derivation of Linear Power Gain

From (9), the amplified signal at the m-th element of TAIS is given as $u_m = \bar{g}_m\, v_m + e_m$. By using the Bussgang theorem, the average linear amplification gain can be written as

$$\begin{aligned}\bar{g}_m &= \frac{\mathbb{E}\{u_m v_m^*\}}{\mathbb{E}\{|v_m|^2\}} = \frac{1}{\rho_m}\mathbb{E}\left\{\sum_{k=0}^{K}\beta_{2k+1}\,|v_m|^{2k+2}\right\}\\ &= \frac{1}{\rho_m}\sum_{k=0}^{K}\beta_{2k+1}\mathbb{E}\left\{|v_m|^{2k+2}\right\}\\ &= \sum_{k=0}^{K}\beta_{2k+1}(k+1)!\rho_m^k. \end{aligned} \tag{66}$$

where the first equation is obtained by substituting $\rho_m = \mathbb{E}(|v_m|^2) = |h_m e^{j\vartheta_m}|^2 P$, and the distortion is uncorrelated with the linear signal, i.e., $\mathbb{E}\{v_m e_m^*\} = 0$.

Appendix B
Derivation of Nonlinear Power Gain

We derive the covariance of the nonlinear distortion based on the Isserlis' theorem [44]. Define the function $\zeta_k : \mathbb{C} \to \mathbb{C}$, $\zeta_k(x) = |x|^{2k}x$. The Isserlis' theorem can be stated as follows.

Theorem 3 (Isserlis' Theorem): For a zero-mean normal random vector, $\boldsymbol{x} = [x_1, \cdots, x_K]^T$, we have

$$\mathbb{E}\left\{\prod_{n=1}^{N} x_n\right\} = \begin{cases} \sum\limits_{\mathcal{V}}\prod\limits_{V_{ij}\in\mathcal{V}}\mathbb{E}\{x_i x_j\} & N \text{ is even},\\ 0 & N \text{ is odd}, \end{cases} \tag{67}$$

where $V_{ij} = \{x_i, x_j\}$ is an arbitrary 2-subset of $\mathcal{X} = \{x_1, \cdots, x_K\}$. $\mathcal{V}$ collects all possible 2-subset partitions of the set $\mathcal{X}$.

Assume $x \sim \mathcal{CN}(0, \sigma_x^2)$ and $y \sim \mathcal{CN}(0, \sigma_y^2)$. Given any two natural numbers k and l, $k, l \in \mathbb{N}$, and the corresponding function $\zeta_k(x)$ and $\zeta_l(x)$ are zero-mean random processes. Let $\mu = \mathbb{E}\{xy^*\}$. Based on Isserlis' theorem [44], the cross-correlation between $\zeta_k(x)$ and $\zeta_l(x)$ is given by

$$\begin{aligned}&\mathbb{E}\{\zeta_k(x)\zeta_l^*(y)\}\\ &= \sum_{a=1}^{\min\{k,l\}}\frac{(k+1)!(l+1)!}{a+1}\binom{k}{a}\binom{l}{a}\sigma_x^{2(k-a)}\sigma_y^{2(l-a)}|\mu|^{2a}\mu. \end{aligned} \tag{68}$$

By substituting (3) and (10) into (11), the distortion term at the m-th element on the TAIS is

$$e_m = \sum_{k=0}^{K} \beta_{2k+1} \left(\zeta_k(v_m) - \rho_m^k (k+1)! \zeta_0(v_m) \right). \tag{69}$$

The cross-correlation between the distortion noise at the m-th and the n-th elements is

$$\begin{aligned}
[\mathbf{C_e}]_{mn} &= \mathbb{E}\left\{ e_m e_n^* \right\} \\
&= \sum_{k=1}^{K} \sum_{l=1}^{K} \beta_{2k+1} \beta_{2l+1}^* \Bigg(\mathbb{E}\left\{ \zeta_k(v_m) \zeta_l^*(v_n) \right\} \\
&\quad - \rho_j^l (l+1)! \mathbb{E}\left\{ \zeta_k(v_m) \zeta_0^*(v_n) \right\} \\
&\quad - P_m^k (k+1)! \mathbb{E}\left\{ \zeta_0(v_m) \zeta_n^*(v_n) \right\} \\
&\quad + \rho_m^k \rho_n^l (k+1)! (l+1)! \mathbb{E}\left\{ \zeta_0(v_m) \zeta_0^*(v_n) \right\} \Bigg).
\end{aligned} \tag{70}$$

By applying (68), the cross-correlation in (70) can be updated as

$$\begin{aligned}
[\mathbf{C_e}]_{mn} &= \sum_{k=1}^{K} \sum_{l=1}^{K} \sum_{a=1}^{\min\{k,l\}} \frac{(k+1)!(l+1)!}{a+1} \binom{k}{a} \binom{l}{a} \\
&\quad \times \beta_{2k+1} \beta_{2l+1}^* \rho_m^{(k-q)} \rho_n^{(l-a)} \left| [\mathbf{C_v}]_{mn} \right|^{2a} [\mathbf{C_v}]_{mn} \\
&= \sum_{a=1}^{K} \sum_{k=a}^{K} \sum_{l=a}^{K} \frac{(k+1)!(l+1)!}{a+1} \binom{k}{a} \binom{l}{a} \\
&\quad \times \beta_{2k+1} \beta_{2l+1}^* \rho_m^{(k-q)} \rho_n^{(l-a)} \left| [\mathbf{C_v}]_{mn} \right|^{2a} [\mathbf{C_v}]_{mn} \\
&= \gamma_k(\rho_m),
\end{aligned} \tag{71}$$

where the second equality is because $\sum_{k=1}^{K} \sum_{l=1}^{K} \sum_{a=1}^{\min\{k,l\}}$ is equivalent to $\sum_{a=1}^{K} \sum_{k=a}^{K} \sum_{l=a}^{K}$.

Appendix C
Proof of Theorem 1

We prove Theorem 1 by leveraging Lemma 1. Define $\mathbf{X}$ and $\mathbf{X}'$ as two positive semi-definite (PSD) matrices with dimension of R. We denote $\mathbf{X}' \succeq \mathbf{X}$, if $\mathbf{X}' - \mathbf{X}$ is a PSD matrix.

Lemma 1: For the following function

$$y(\mathbf{X}) = \log_2 \det \left(\mathbf{I} + \left(\omega_2 \mathbf{X} + \mathbf{I} \right)^{-1} \omega_1 \mathbf{X} \right), \tag{72}$$

if $\mathbf{X}' \succeq \mathbf{X}$, *we have* $y(\mathbf{X}') \geq y(\mathbf{X})$.

Proof: Rearrange the eigenvalues of $\mathbf{X}$ and $\mathbf{X}'$ in descending order, $\lambda_1 \geq \cdots \geq \lambda_r$ and $\lambda_1' \geq \cdots \geq \lambda_r'$, respectively. By the condition that $\mathbf{X}' \succ \mathbf{X}$, for each eigenvalue of $\mathbf{X}$ and $\mathbf{X}'$, we have $\lambda_r \geq \lambda_r'$ for $r = 1, \cdots, R$. $y(\mathbf{X})$ can be equivalently expressed as

$$y(\mathbf{X}) = \sum_{r=1}^{R} \log_2 \left(1 + \frac{\omega_1 \lambda_r}{\omega_2 \lambda_r + 1} \right), \tag{73}$$

which is a non-decreasing function of λ_r. Therefore, we have $y(\mathbf{X}') \geq y(\mathbf{X})$, since $\lambda_r \geq \lambda_r'$, $\forall r = \{1, \cdots, R\}$. □

From (19), we have $\mathbf{C_v} = \rho \boldsymbol{\Theta} \overline{\mathbf{h}\mathbf{h}}^{\mathrm{H}} \boldsymbol{\Theta}^{\mathrm{H}} = \rho \overline{\mathbf{w}\mathbf{w}}^{\mathrm{H}}$. We denote $\overline{\mathbf{w}} = \boldsymbol{\Theta}\overline{\mathbf{h}}$, which is a vector with constant modulus entries, i.e., $|\overline{\mathbf{w}}|_m = \sqrt{1/M}$. Since the input power of each PA is equal to ρ, we have the matrix of the average linear gain as $\overline{\mathbf{G}} = \overline{g}(\rho) \mathbf{I}_M$, and the power of the desired signal after the amplification (as shown in the numerator in the SE expression (15)) is given by

$$\overline{\mathbf{G}} \mathbf{C_v} \overline{\mathbf{G}}^{\mathrm{H}} = \overline{\gamma}_s(\rho) \rho \, \boldsymbol{\Theta} \mathbf{h} \mathbf{h}^{\mathrm{H}} \boldsymbol{\Theta}^{\mathrm{H}} = \overline{\gamma}_s(\rho) \rho \overline{\mathbf{w}\mathbf{w}}^{\mathrm{H}}, \tag{74}$$

where $\overline{\gamma}_s(\rho) \triangleq |\overline{g}(\rho)|^2$, as (24). The covariance matrix of the distortion in (12) is updated as

$$\begin{aligned}
\mathbf{C_e} &= \sum_{k=1}^{K} \boldsymbol{\Gamma}_k \mathbf{C_v} \odot \left| \mathbf{C_v} \right|^{2k} \boldsymbol{\Gamma}_k^{\mathrm{H}} = \sum_{k=1}^{K} |\gamma_k(\rho)|^2 \rho^{2k} \mathbf{C_v} \\
&= \overline{\gamma}_e(\rho) \rho \overline{\mathbf{w}\mathbf{w}}^{\mathrm{H}}.
\end{aligned} \tag{75}$$

It is observed that the desired signal and distortion have the same spatial directivity.

By substituting the ω_1 and ω_2 in (72) with $\overline{\gamma}_s(\rho) \rho / N_0$ and $\overline{\gamma}_e(\rho) \rho / N_0$, respectively, the SE in (15) can be written as $SE = y(\mathbf{F}\mathbf{C_v}\mathbf{F}^{\mathrm{H}})$, where the function $y(\cdot)$ is defined in Lemma 1. $\rho \overline{\mathbf{F}\mathbf{F}}^{\mathrm{H}} \succeq \mathbf{F}\mathbf{C_v}\mathbf{F}^{\mathrm{H}}$ holds for any $\mathbf{C_v} = \rho \boldsymbol{\Theta} \mathbf{h} \mathbf{h}^{\mathrm{H}} \boldsymbol{\Theta}^{\mathrm{H}}$, when the power constraint $tr(\mathbf{C_v}) \leq \rho$ is met. Based on Lemma 1, we have $y(\rho \overline{\mathbf{F}\mathbf{F}}^{\mathrm{H}}) \geq y(\mathbf{F}\mathbf{C_v}\mathbf{F}^{\mathrm{H}})$. It concludes that the maximum spectral efficiency is $\overline{SE} = y(\rho \overline{\mathbf{F}\mathbf{F}}^{\mathrm{H}})$, where the equality is achieved if $\boldsymbol{\Theta}\overline{\mathbf{h}} = \mathbf{a}_{\mathrm{TAIS}}(\psi_{\max}^{S_t}, \phi_{\max}^{S_t})$.

Appendix D
Proof of Corollary 1

We prove Corollary 1 by leveraging Lemma 2 as follows. Define a positive semi-definite matrix $\mathbf{X}$ in R dimension, and a complex-value vector $\mathbf{a} \in \mathbb{C}^R$, which satisfies $\mathbf{a}^{\mathrm{H}}\mathbf{a} = 1$.

Lemma 2: With $y(\mathbf{X})$ *defined in Lemma 1, for the function*

$$z(\mathbf{X}, \mathbf{a}) = \log_2 \left(1 + \frac{\omega_1 \mathbf{a}^{\mathrm{H}} \mathbf{X} \mathbf{a}}{\omega_2 \mathbf{a}^{\mathrm{H}} \mathbf{X} \mathbf{a} + 1} \right), \tag{76}$$

$y(\mathbf{X}) \geq z(\mathbf{X}, \mathbf{a})$ *always holds, where the equality holds if and only if* $\mathbf{X}$ *is a rank-one matrix and* $\mathbf{a}$ *corresponds to the eigenvector of* $\mathbf{X}$ *with a non-zero eigenvalue.*

Proof: Rearrange the eigenvalues of $\mathbf{X}$ in descending order, $\lambda_1 \geq \cdots \geq \lambda_r$. As λ_1 is the maximum eigenvalues of $\mathbf{X}$, we have $\mathbf{a}^{\mathrm{H}}\mathbf{X}\mathbf{a} \leq \max_{\mathbf{a}} \mathbf{a}^{\mathrm{H}}\mathbf{X}\mathbf{a} = \lambda_1$, where the equality holds when $\mathbf{a}$ matches the eigenvector of $\mathbf{X}$ corresponding to maximum eigenvalues of $\mathbf{X}$. Since $\log_2 \left(1 + \frac{\omega_1 \lambda_r}{\omega_2 \lambda_r + 1} \right)$ in (73) is a non-decreasing function of λ_r, the equation (76) satisfies

$$\begin{aligned}
z(\mathbf{X}, \mathbf{a}) &\leq \log_2 \left(1 + \frac{\omega_1 \lambda_1}{\omega_2 \lambda_1 + 1} \right) \\
&\leq \sum_{r=1}^{R} \log_2 \left(1 + \frac{\omega_1 \lambda_r}{\omega_2 \lambda_r + 1} \right) \\
&= y(\mathbf{X}),
\end{aligned} \tag{77}$$

where the equality is obtained by (73). When $\mathbf{X}$ is a rank-one matrix, $\lambda_r = 0$, $r > 1$, which guarantees the second inequality

in (77). When $\mathbf{a}$ is the eigenvector corresponding to the only non-zero eigenvalue of $\mathbf{X}$, the first inequality in (77) holds, which completes the proof. □

By substituting $\omega_1 = \overline{\gamma}_s(\rho)\rho/N_0$ and $\omega_2 = \overline{\gamma}_e(\rho)\rho/N_0$ in (76), and $\mathbf{X} = \rho\overline{\mathbf{F}\mathbf{F}}^{\mathrm{H}}$, we have $\overline{SE} = y(\rho\overline{\mathbf{F}\mathbf{F}}^{\mathrm{H}})$, where the function $y(\cdot)$ is defined in Lemma 1. Given $\mathbf{a}_{\max} = \mathbf{a}_{\mathrm{BS}}(\psi^B_{\max}, \phi^B_{\max})^{\mathrm{H}}$ as the vector corresponding to the maximum eigenvalues of $\rho\overline{\mathbf{F}\mathbf{F}}^{\mathrm{H}}$, we have

$$z(\rho\overline{\mathbf{F}\mathbf{F}}^{\mathrm{H}}, \mathbf{a}_{\max})) \leq y(\rho\overline{\mathbf{F}\mathbf{F}}^{\mathrm{H}}) = \overline{SE}, \tag{78}$$

where the left-hand side of (78) establishes the lower bound of the maximum spectral efficiency as given in (36).

REFERENCES

[1] W. Chen, J. Montojo, J. Lee, M. Shafi, and Y. Kim, "The standardization of 5G-advanced in 3GPP," *IEEE Commun. Mag.*, vol. 60, no. 11, pp. 98–104, Nov. 2022.

[2] W. Tang et al., "Wireless communications with programmable metasurface: New paradigms, opportunities, and challenges on transceiver design," *IEEE Wireless Commun.*, vol. 27, no. 2, pp. 180–187, Apr. 2020.

[3] J. Zhang, J. Liu, S. Ma, C.-K. Wen, and S. Jin, "Large system achievable rate analysis of RIS-assisted MIMO wireless communication with statistical CSIT," *IEEE Trans. Wireless Commun.*, vol. 20, no. 9, pp. 5572–5585, Sep. 2021.

[4] M. Matthaiou, O. Yurduseven, H. Q. Ngo, D. Morales-Jimenez, S. L. Cotton, and V. F. Fusco, "The road to 6G: Ten physical layer challenges for communications engineers," *IEEE Commun. Mag.*, vol. 59, no. 1, pp. 64–69, Jan. 2021.

[5] A. Schumacher, R. Merz, and A. Burg, "Adding indoor capacity without fiber backhaul: An mmWave bridge prototype," *IEEE Commun. Mag.*, vol. 59, no. 4, pp. 110–115, Apr. 2021.

[6] M. Giordani, M. Polese, A. Roy, D. Castor, and M. Zorzi, "Standalone and non-standalone beam management for 3GPP NR at mmWaves," *IEEE Commun. Mag.*, vol. 57, no. 4, pp. 123–129, Apr. 2019.

[7] *Study on Channel Model for Frequencies From 0.5 to 100 GHz*, 3GPP, document 38.901, Jan. 2020.

[8] *Study on XR (Extended Reality) Evaluations for NR*, document 38.838, Dec. 2021.

[9] X. Liu, Y. Liu, Y. Chen, and H. V. Poor, "RIS enhanced massive non-orthogonal multiple access networks: Deployment and passive beamforming design," *IEEE J. Sel. Areas Commun.*, vol. 39, no. 4, pp. 1057–1071, Apr. 2021.

[10] M. Di Renzo et al., "Smart radio environments empowered by reconfigurable intelligent surfaces: How it works, state of research, and the road ahead," *IEEE J. Sel. Areas Commun.*, vol. 38, no. 11, pp. 2450–2525, Nov. 2020.

[11] Q. Wu and R. Zhang, "Towards smart and reconfigurable environment: Intelligent reflecting surface aided wireless network," *IEEE Commun. Mag.*, vol. 58, no. 1, pp. 106–112, Jan. 2020.

[12] W. Tang et al., "Path loss modeling and measurements for reconfigurable intelligent surfaces in the millimeter-wave frequency band," *IEEE Trans. Commun.*, vol. 70, no. 9, pp. 6259–6276, Sep. 2022.

[13] M. Nemati, B. Maham, S. R. Pokhrel, and J. Choi, "Modeling RIS empowered outdoor-to-indoor communication in mmWave cellular networks," *IEEE Trans. Commun.*, vol. 69, no. 11, pp. 7837–7850, Nov. 2021.

[14] M. Najafi, V. Jamali, R. Schober, and H. V. Poor, "Physics-based modeling and scalable optimization of large intelligent reflecting surfaces," *IEEE Trans. Commun.*, vol. 69, no. 4, pp. 2673–2691, Apr. 2021.

[15] Q. Wu and R. Zhang, "Intelligent reflecting surface enhanced wireless network via joint active and passive beamforming," *IEEE Trans. Wireless Commun.*, vol. 18, no. 11, pp. 5394–5409, Nov. 2019.

[16] W. Tang et al., "MIMO transmission through reconfigurable intelligent surface: System design, analysis, and implementation," *IEEE J. Sel. Areas Commun.*, vol. 38, no. 11, pp. 2683–2699, Nov. 2020.

[17] R. Long, Y.-C. Liang, Y. Pei, and E. G. Larsson, "Active reconfigurable intelligent surface-aided wireless communications," *IEEE Trans. Wireless Commun.*, vol. 20, no. 8, pp. 4962–4975, Aug. 2021.

[18] Z. Zhang et al., "Active RIS vs. passive RIS: Which will prevail in 6G?" *IEEE Trans. Commun.*, vol. 71, no. 3, pp. 1707–1725, Mar. 2023.

[19] S. S. Luo, Y. Ruan, and L. Chen, "Optical-transparent metasurface for flexible manipulation and analog information modulation," *Opt. Exp.*, vol. 29, no. 4, pp. 5867–5876, 2021.

[20] W. Su et al., "Printing flexible terahertz metasurface of optical transparency," *J. Phys. D, Appl. Phys.*, vol. 52, no. 9, Feb. 2019, Art. no. 095107.

[21] D. Kitayama, Y. Hama, K. Goto, K. Miyachi, T. Motegi, and O. Kagaya, "Transparent dynamic metasurface for a visually unaffected reconfigurable intelligent surface: Controlling transmission/reflection and making a window into an RF lens," *Opt. Exp.*, vol. 29, no. 18, pp. 29292–29307, 2021.

[22] J. Aumentado, "Superconducting parametric amplifiers: The state of the art in Josephson parametric amplifiers," *IEEE Microw. Mag.*, vol. 21, no. 8, pp. 45–59, Aug. 2020.

[23] N. T. Nguyen, Q.-D. Vu, K. Lee, and M. Juntti, "Hybrid relay-reflecting intelligent surface-assisted wireless communications," *IEEE Trans. Veh. Technol.*, vol. 71, no. 6, pp. 6228–6244, Jun. 2022.

[24] C. Feng, W. Shen, J. An, and L. Hanzo, "Joint hybrid and passive RIS-assisted beamforming for mmWave MIMO systems relying on dynamically configured subarrays," *IEEE Internet Things J.*, vol. 9, no. 15, pp. 13913–13926, Aug. 2022.

[25] A. H. A. Bafghi, V. Jamali, M. Nasiri-Kenari, and R. Schober, "Degrees of freedom of the K-user interference channel assisted by active and passive IRSs," *IEEE Trans. Commun.*, vol. 70, no. 5, pp. 3063–3080, May 2022.

[26] R. Deng, B. Di, H. Zhang, Y. Tan, and L. Song, "Reconfigurable holographic surface-enabled multi-user wireless communications: Amplitude-controlled holographic beamforming," *IEEE Trans. Wireless Commun.*, vol. 21, no. 8, pp. 6003–6017, Aug. 2022.

[27] K. Liu, Z. Zhang, L. Dai, S. Xu, and F. Yang, "Active reconfigurable intelligent surface: Fully-connected or sub-connected?" *IEEE Commun. Lett.*, vol. 26, no. 1, pp. 167–171, Jan. 2022.

[28] S. Taravati and G. V. Eleftheriades, "Full-duplex reflective beamsteering metasurface featuring magnetless nonreciprocal amplification," *Nature Commun.*, vol. 12, no. 1, pp. 1–11, Jul. 2021.

[29] X. Wang, J. Han, S. Tian, D. Xia, L. Li, and T. J. Cui, "Amplification and manipulation of nonlinear electromagnetic waves and enhanced nonreciprocity using transmissive space-time-coding metasurface," *Adv. Sci.*, vol. 9, no. 11, Apr. 2022, Art. no. 2105960.

[30] A. K. Popov and V. M. Shalaev, "Negative-index metamaterials: Second-harmonic generation, Manley–Rowe relations and parametric amplification," *Appl. Phys. B, Lasers Opt.*, vol. 84, nos. 1–2, pp. 131–137, Jul. 2006.

[31] E. Zedini, A. Kammoun, and M.-S. Alouini, "Performance of multibeam very high throughput satellite systems based on FSO feeder links with HPA nonlinearity," *IEEE Trans. Wireless Commun.*, vol. 19, no. 9, pp. 5908–5923, Sep. 2020.

[32] J. B. King and T. J. Brazil, "Nonlinear electrothermal GaN HEMT model applied to high-efficiency power amplifier design," *IEEE Trans. Microw. Theory Techn.*, vol. 61, no. 1, pp. 444–454, Jan. 2013.

[33] N. N. Moghadam, G. Fodor, M. Bengtsson, and D. J. Love, "On the energy efficiency of MIMO hybrid beamforming for millimeter-wave systems with nonlinear power amplifiers," *IEEE Trans. Wireless Commun.*, vol. 17, no. 11, pp. 7208–7221, Nov. 2018.

[34] E. Björnson, L. Sanguinetti, and J. Hoydis, "Hardware distortion correlation has negligible impact on UL massive MIMO spectral efficiency," *IEEE Trans. Commun.*, vol. 67, no. 2, pp. 1085–1098, Feb. 2019.

[35] Y. Hmamouche, M. Benjillali, and S. Saoudi, "Fresnel line-of-sight probability with applications in airborne platform-assisted communications," *IEEE Trans. Veh. Technol.*, vol. 71, no. 5, pp. 5060–5072, May 2022.

[36] 3GPP. (2017). *Study on Channel Model for Frequencies From 0.5 to 100 GHz*. [Online]. Available: https://www.3gpp.org/DynaReport/38901.htm

[37] X. Cai, Y. Miao, J. Li, F. Tufvesson, G. F. Pedersen, and W. Fan, "Dynamic mmWave channel emulation in a cost-effective MPAC with dominant-cluster concept," *IEEE Trans. Antennas Propag.*, vol. 70, no. 6, pp. 4691–4704, Jun. 2022.

[38] T. Lipp and S. Boyd, "Variations and extension of the convex–concave procedure," *Optim. Eng.*, vol. 17, no. 2, pp. 263–287, Jun. 2016.

[39] D. Persson, T. Eriksson, and E. G. Larsson, "Amplifier-aware multiple-input multiple-output power allocation," *IEEE Commun. Lett.*, vol. 17, no. 6, pp. 1112–1115, Jun. 2013.

[40] C. Huang, A. Zappone, G. C. Alexandropoulos, M. Debbah, and C. Yuen, "Reconfigurable intelligent surfaces for energy efficiency in wireless communication," *IEEE Trans. Wireless Commun.*, vol. 18, no. 8, pp. 4157–4170, Aug. 2019.

[41] S. Rezaei Aghdam, S. Jacobsson, U. Gustavsson, G. Durisi, C. Studer, and T. Eriksson, "Distortion-aware linear precoding for massive MIMO downlink systems with nonlinear power amplifiers," 2020, *arXiv:2012.13337*.

[42] *RF WebLab*. Accessed: Sep. 29, 2022. [Online]. Available: http://dpdcompetition.com/rfweblab/

[43] R. A. Tasci, F. Kilinc, E. Basar, and G. C. Alexandropoulos, "A new RIS architecture with a single power amplifier: Energy efficiency and error performance analysis," *IEEE Access*, vol. 10, pp. 44804–44815, 2022.

[44] L. Isserlis, "On a formula for the product-moment coefficient of any order of a normal frequency distribution in any number of variables," *Biometrika*, vol. 12, nos. 1–2, pp. 134–139, Nov. 1918.

Bin Liu (Student Member, IEEE) is currently pursuing the Ph.D. degree in electrical engineering with KU Leuven, Belgium. From March 2022 to October 2022, he was a Visiting Scholar with the Delft University of Technology, The Netherlands. His research interests include signal processing in massive MIMO, reconfigurable intelligent surfaces, and mmWave communications. He was awarded the Best Paper Award from the IEEE ICC 2023.

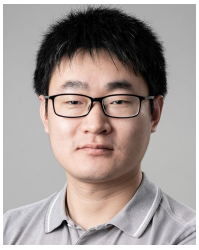

Qing Wang (Senior Member, IEEE) received the Ph.D. degree from the University Carlos III of Madrid (UC3M) and IMDEA Networks Institute, Spain, in 2016. He is currently an Assistant Professor with the Embedded Systems Group, Delft University of Technology, The Netherlands. He is also the Co-Founder of OpenVLC, an open-source and low-cost platform for VLC research. His research interests include visible light communication and sensing systems, and embedded AI for the Internet of Things. He has received several paper awards, including the Best Paper Awards from ICC'23, EWSN'23, SenSys'22, Morse'22, and COMSNETS'19, and the Best Paper Runner-Up Award from EWSN'22, MobiCom'20 (Honourable Mention), and CoNEXT'16.

Sofie Pollin (Senior Member, IEEE) is currently a Professor at KU Leuven, Belgium, with a focus on wireless communication systems. Before that, she worked at imec and UC Berkeley, and she is currently a Principal Member of technical staff at imec. Her research centers around wireless networks that require networks that are ever more dense, heterogeneous, battery powered, and spectrum constrained. Her research interests are cell-free networks, integrated communication and sensing, and non-terrestrial networks.